Sensor noise in *LISA Pathfinder*: An extensive in-flight review of the angular and longitudinal interferometric measurement system

M. Armano,[1] H. Audley,[2,3] J. Baird,[4] P. Binetruy,[4,*] M. Born,[2,3] D. Bortoluzzi,[5] N. Brandt,[6] E. Castelli,[7] A. Cavalleri,[8] A. Cesarini,[9] A. M. Cruise,[10] K. Danzmann,[2,3] M. de Deus Silva,[11] I. Diepholz,[2,3] G. Dixon,[10] R. Dolesi,[7] L. Ferraioli,[12] V. Ferroni,[7] E. D. Fitzsimons,[13] R. Flatscher,[6] M. Freschi,[11] A. García,[14] R. Gerndt,[6] L. Gesa,[15,16,†] D. Giardini,[12] F. Gibert,[7,17] R. Giusteri,[2,3] C. Grimani,[9] J. Grzymisch,[1] F. Guzman,[18] I. Harrison,[19] M-S Hartig,[2,3] G. Hechenblaikner,[6] G. Heinzel,[2,3,¶] M. Hewitson,[2,3,**] D. Hollington,[20] D. Hoyland,[10] M. Hueller,[7] H. Inchauspé,[4,21] O. Jennrich,[1] P. Jetzer,[22] U. Johann,[6] B. Johlander,[1] N. Karnesis,[4] B. Kaune,[2,3] C. J. Killow,[23] N. Korsakova,[24] J. A. Lobo,[15,16,‡] J. P. López-Zaragoza,[15] R. Maarschalkerweerd,[19] D. Mance,[12] V. Martín,[15,16] L. Martin-Polo,[11] F. Martin-Porqueras,[11] J. Martino,[4] P. W. McNamara,[1] J. Mendes,[19] L. Mendes,[11] N. Meshksar,[12] A. Monsky,[25] M. Nofrarias,[15,16] S. Paczkowski,[2,3,‖] M. Perreur-Lloyd,[23] A. Petiteau,[4] E. Plagnol,[4] J. Ramos-Castro,[26,16] J. Reiche,[2,3] F. Rivas,[27] D. I. Robertson,[23,††] G. Russano,[7] J. Sanjuan,[28] J. Slutsky,[29] C. F. Sopuerta,[15,16] F. Steier,[25] T. Sumner,[20] D. Texier,[11] J. I. Thorpe,[29] D. Vetrugno,[7] S. Vitale,[7] V. Wand,[25] G. Wanner,[2,3] H. Ward,[23] P. J. Wass,[20,21] W. J. Weber,[7] L. Wissel,[2,3,§] A. Wittchen,[2,3] and P. Zweifel[12]

[1]*European Space Technology Centre, European Space Agency, Keplerlaan 1, 2200 AG Noordwijk, Netherlands*
[2]*Max Planck Institute for Gravitational Physics (Albert-Einstein-Institut), 30167 Hannover, Germany*
[3]*Leibniz Universität Hannover, 30167 Hannover, Germany*
[4]*APC, Université de Paris, CNRS, Astroparticule et Cosmologie, F-75006 Paris, France*
[5]*Department of Industrial Engineering, University of Trento, via Sommarive 9, 38123 Trento, Italy and Trento Institute for Fundamental Physics and Application/INFN, 38123 Povo, Trento, Italy*
[6]*Airbus Defence and Space, Claude-Dornier-Strasse, 88090 Immenstaad, Germany*
[7]*Dipartimento di Fisica, Università di Trento and Trento Institute for Fundamental Physics and Application / INFN, 38123 Povo, Trento, Italy*
[8]*Istituto di Fotonica e Nanotecnologie, CNR-Fondazione Bruno Kessler, I-38123 Povo, Trento, Italy*
[9]*DISPEA, Università di Urbino Carlo Bo, Via S. Chiara, 27 61029 Urbino/INFN, Italy*
[10]*The School of Physics and Astronomy, University of Birmingham, B15 2TT Birmingham, United Kingdom*
[11]*European Space Astronomy Centre, European Space Agency, Villanueva de la Cañada, 28692 Madrid, Spain*
[12]*Institut für Geophysik, ETH Zürich, Sonneggstrasse 5, CH-8092 Zürich, Switzerland*
[13]*The UK Astronomy Technology Centre, Royal Observatory, Edinburgh, Blackford Hill, Edinburgh EH9 3HJ, United Kingdom*
[14]*City University of Applied Sciences, Flughafenallee 10, 28199 Bremen, Germany*
[15]*Institut de Ciències de l'Espai (ICE, CSIC), Campus UAB, Carrer de Can Magrans s/n, 08193 Cerdanyola del Vallès, Spain*
[16]*Institut d'Estudis Espacials de Catalunya (IEEC), C/ Gran Capità 2-4, 08034 Barcelona, Spain*
[17]*isardSAT SL, Marie Curie 8-14, 08042 Barcelona, Catalonia, Spain*
[18]*Texas A&M University, 701 H.R. Bright Bldg, College Station, Texas 77843-3141, USA*
[19]*European Space Operations Centre, European Space Agency, 64293 Darmstadt, Germany*
[20]*High Energy Physics Group, Physics Department, Imperial College London, Blackett Laboratory, Prince Consort Road, London SW7 2BW, United Kingdom*
[21]*Department of Mechanical and Aerospace Engineering, MAE-A, P.O. Box 116250, University of Florida, Gainesville, Florida 32611, USA*
[22]*Physik Institut, Universität Zürich, Winterthurerstrasse 190, CH-8057 Zürich, Switzerland*
[23]*SUPA, Institute for Gravitational Research, School of Physics and Astronomy, University of Glasgow, Glasgow G12 8QQ, United Kingdom*
[24]*Observatoire de la Côte d'Azur, Boulevard de l'Observatoire CS 34229-F, 06304 NICE, France*
[25]*OHB System AG, Universitätsallee 27-29, 28359 Bremen, Germany*
[26]*Department d'Enginyeria Electrònica, Universitat Politècnica de Catalunya, 08034 Barcelona, Spain*

[27]*Department of Quantitative Methods, Universidad Loyola Andalucia, Avenida de las Universidades s/n, 41704 Dos Hermanas, Sevilla, Spain*
[28]*Department of Physics, 2001 Museum Road, University of Florida, Gainesville, Florida 32611, USA*
[29]*Gravitational Astrophysics Lab, NASA Goddard Space Flight Center, 8800 Greenbelt Road, Greenbelt, Maryland 20771, USA*

(Received 30 June 2022; accepted 27 July 2022; published 3 October 2022)

In a previous article [1], we have reported on the first subpicometer interferometer flown in space as part of ESA's LISA Pathfinder mission, and have shown the residual sensor noise to be on the level of $32.0^{+2.4}_{-1.7}$ fm/$\sqrt{\text{Hz}}$. This review provides a deeper and more complete overview of the full system and its interferometric mission performance under varying operational conditions, allowing a much more detailed view on the noise model. We also include the optical measurements of rotations through differential wave front sensing (DWS), which reached a sensitivity of as good as 100 prad/$\sqrt{\text{Hz}}$. We present more evidence for the long-term stability of the interferometric performance and components. This proves a solid foundation for future interferometry in space such as the LISA mission.

DOI: 10.1103/PhysRevD.106.082001

I. INTRODUCTION

LISA Pathfinder (LPF) [1–18] was a European Space Agency (ESA) mission launched on December 3rd, 2015 with a VEGA launcher from Kourou, French Guiana. It was designed as a technology demonstrator for future space-based laser-interferometric gravitational wave detectors, in particular the Laser Interferometer Space Antenna (LISA) [19]. The core of the experiment was two free-floating test masses (TMs), one of which was used as a drag-free reference for the spacecraft and the other as a quiet reference. The primary objective of the mission was to verify and analyze in detail the performance of the free-falling TMs at a level of spurious accelerations below 3×10^{-14} ms^{-2}/$\sqrt{\text{Hz}}$ at mHz frequencies.

An essential element of the associated drag-free control of the Spacecraft (SC) was the laser interferometric optical readout of the position and orientation of both TMs at a design noise level of a few pm/$\sqrt{\text{Hz}}$ and nrad/$\sqrt{\text{Hz}}$. This system, called the Optical Metrology System (OMS), represents the first precision laser interferometer operated in space. While the main results of the LISA Pathfinder mission have been reported in [12,13] and the subpicometer performance of the OMS longitudinal TM readout has been published in [1], this paper provides extensive details of the OMS design and in-flight performance across all degrees-of-freedom and under varying conditions from very low to very high contrast. We show that the sensitivity has been better than the requirements throughout the mission and would be sufficient for the local metrology of a LISA-like mission.

After achieving all objectives and a mission extension, the SC was finally turned off on July 18, 2017 and is now orbiting freely and unobserved in the inner solar system.

Please note that we provide additional descriptions of interferometer readouts and acronyms in Appendixes A and C to support the reader.

II. THE OPTICAL METROLOGY SUBSYSTEM

The purpose of the OMS was to continuously monitor, with low noise, the position and orientation of both TMs with respect to each other and to the spacecraft. These measurements were then used as input for the drag-free and attitude control system (DFACS) of the spacecraft, which included the suspension controller that maintains the second (reference) TM at the optimal working point [12,17,20]. The OMS output was also the primary measurement used to derive the residual differential acceleration of the TMs [14].

The optics of the OMS were mounted on an optical bench (OB) located between the two TMs and rigidly fixed to the spacecraft frame. The OMS directly measured six degrees of freedom, namely the variations in separation of the two TMs, x_{12}, the variation in separation of the first TM to the OB, x_1, and the corresponding pitch and yaw angles ϕ_{12}, η_{12} (differential tilts between the TMs), and ϕ_1, η_1 (relative tilt of TM1 to the OB). Linear combinations of these measurements provided the position and orientation of the second TM with respect to the OB, x_2, ϕ_2, and η_2 (see Fig. 1).

*Deceased 30 March 2017.
†Deceased 29 May 2020.
‡Deceased 30 September 2012.
§lennart.wissel@aei.mpg.de
‖sarah.paczkowski@aei.mpg.de
¶gerhard.heinzel@aei.mpg.de
**martin.hewitson@aei.mpg.de
††david.robertson@glasgow.ac.uk

Published by the American Physical Society under the terms of the Creative Commons Attribution 4.0 International license. Further distribution of this work must maintain attribution to the author(s) and the published article's title, journal citation, and DOI. Open access publication funded by the Max Planck Society.

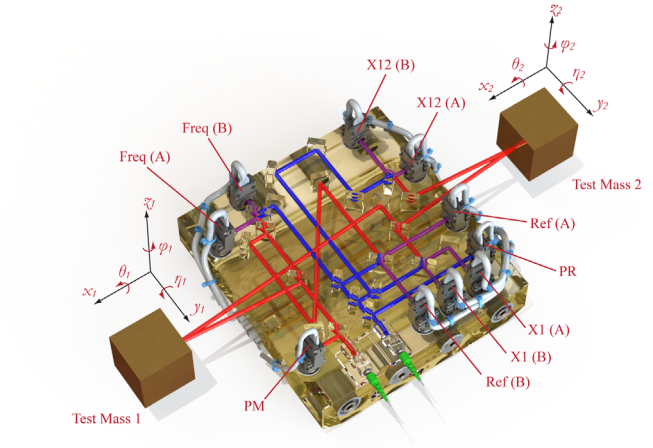

FIG. 1. Distances and angles measured by the OMS. This CAD model of the optical bench traces the paths of the two beams. The various photodiodes are labeled according to their interferometer name and are labeled (A) and (B) for the two output ports of each recombination beamsplitter. Slightly modified from [1], with corrected X12 diode labels; PM power measurement diode for the measurement beam, and PR power measurement diode for the reference beam.

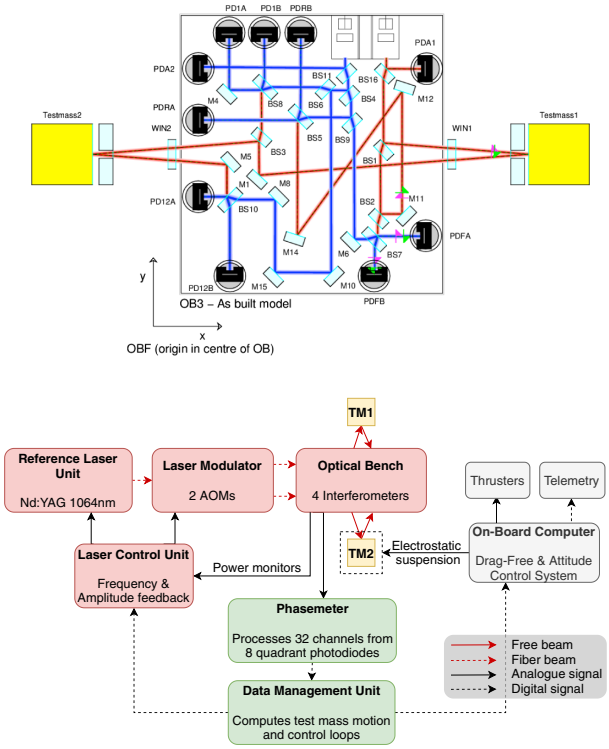

FIG. 2. Top panel: The four interferometers on the OB. The Optical Bench Frame (OBF) has its origin in the center of the OB. Bottom panel: Schematic overview of the OMS and its main components (reprint from [1] for convenience).

A. Requirements and environment

While the TMs were designed to be shielded from external forces and thus were very quiet, they could move by more than one laser wavelength such that one fundamental requirement on the OMS was the ability to track x_1 and x_{12} with constant sensitivity over more than one wavelength ("fringe").

In the initial design phase, the TM displacement noise requirement for the OMS was set at 9 $\mathrm{pm}/\sqrt{\mathrm{Hz}} \times \mathrm{NSF}(f)$ for x_1 and x_{12}, where $\mathrm{NSF}(f) = \sqrt{1 + (3\ \mathrm{mHz}/f)^4}$ is the noise shape function adapted to the expected cross-over between force noise induced TM motion and interferometric sensing noise. The required measurement band was $1\ \mathrm{mHz} < f < 30\ \mathrm{mHz}$.

The requirement for the measurement noise of ϕ_{12}, η_{12}, ϕ_1, and η_1 was $20\ \mathrm{nrad}/\sqrt{\mathrm{Hz}} \times \mathrm{NSF}(f)$ in the same band [21,22].

LPF was operated in a very quiet and stable Lissajous orbit around the Earth-Sun Lagrange point L1, about 1.5 million km from the Earth and at a nearly constant separation and orientation with respect to the Sun. This led to a very stable thermal and mechanical environment, better than what is possible to achieve on Earth.

B. Basic design and subsystems

Due to the requirement of tracking more than one fringe, the basic OMS design was a set of heterodyne Mach-Zehnder-derived interferometers all operating at the same fixed frequency difference of $f_{\mathrm{het}} = 1$ kHz [23–25]. A single Nd:YAG NPRO laser delivered light with a wavelength of 1064 nm through a polarization-maintaining fiber to the modulation unit, where it was split into two parts, each of which was frequency-shifted by acousto-optic modulators (AOMs), operating at frequencies f_1 and f_2, respectively. While $f_1 \approx f_2 \approx 80$ MHz, their difference is fixed to the preselected heterodyne frequency; $f_1 - f_2 = f_{\mathrm{het}} = 1$ kHz.

That difference between the modulation frequencies f_{het} was locked with a phase locked loop (PLL) to a reference frequency generated by the Data Management Unit (DMU), which served as the data processing unit for the OMS. A piezo actuator in each beam in the modulation unit was used to control the phase difference between both beams on the optical bench. The light was delivered to the OB through two optical fibers, one for each frequency, to serve as "Measurement beam" (red traces in Figs. 2 and 3) and "Reference beam" (blue traces in Figs. 2 and 3), respectively. Fiber couplers mounted on the optical bench produced collimated nearly Gaussian beams with a diameter ($2\omega_0$) of approximately 1.2 mm and in addition performed polarization cleaning. On the OB there were four separate interferometers (see Figs. 2 and 3) that measured:

(i) x_1, ϕ_1, and η_1, i.e., the position and orientation of TM1 with respect to the OB, called the "X1" interferometer;

(ii) x_{12}, $\phi_{12} = \phi_2 - \phi_1$, and $\eta_{12} = \eta_2 - \eta_1$, i.e., the separation between the two TM and the difference of their orientations, called the "X12" interferometer;

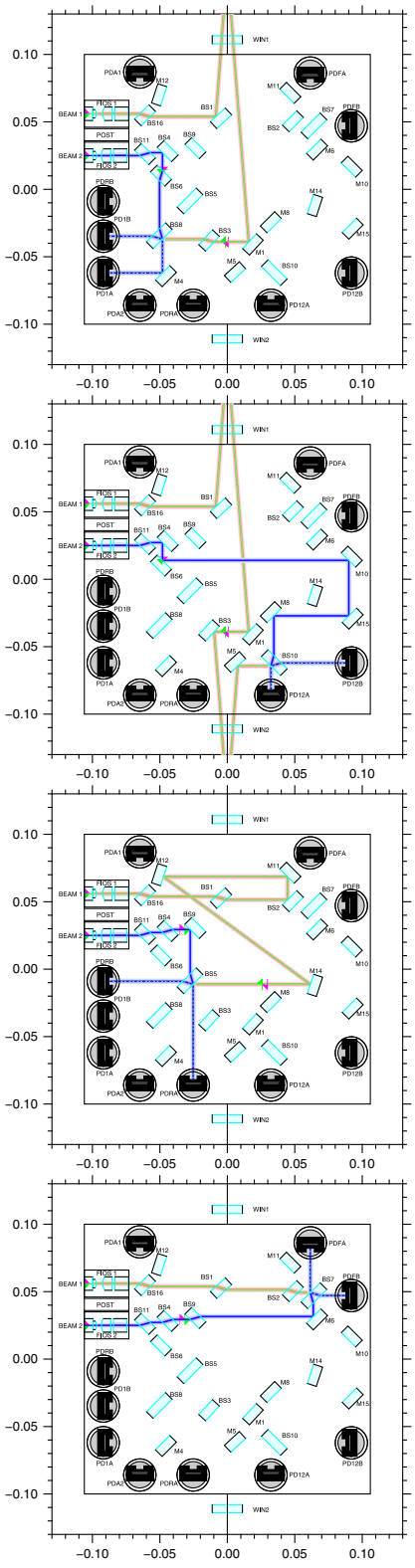

FIG. 3. The four interferometers on the OB shown separately. TM1 is above the top, TM2 below the bottom of each picture. From top to bottom: X1, X12, Reference, Frequency interferometer. The scale is given in meters. Note that the layout is rotated by 90° compared to Fig. 2.

(iii) x_R, the phase difference of the two beams on the OB without interaction with the TMs. It measures any unwanted relative phase noise between the two beams that is accumulated in the optical paths through the AOMs and optical fiber links leading to the OB. Thus, it is used as a phase reference for the X1 and X12 interferometers and additionally as an error signal for the optical path length difference (OPD) stabilization loop explained below in Sec. II C. This interferometer is called "XR" for reference;

(iv) x_F, another TM independent phase difference but with an intentional path length difference of (38.2 ± 0.1) cm [26] between the two arms, serving as a laser-frequency noise sensor and called "XF" for "frequency".

The four interferometers were balanced in terms of beam powers, the number of reflections and transmissions in beam splitters each beam undergoes before interference, and in terms of optical path lengths, with the intentional exception of the frequency interferometer. In order to make the OB as compact as possible, this was achieved by moving part of the common optical path of the reference beam into the optical fiber of that beam, which was around 38 cm longer than its counterpart for the measurement beam.

Each of the four beam combiners has two complementary output ports, which were directed to a total of eight InGaAs quadrant photodiodes (QPDs) with a diameter of 5 mm. The photocurrent in each photodiode was dominated by a strong sinusoidal component at f_{het}, the phase of which encodes the path length difference between the reference and measurement beams. The second port of each beam splitter had the same signal with a phase shift of π (the two outputs port photodiodes for the X1 interferometer, for example, are PD1A and PD1B in the upper panel of Fig. 2). The TM angles were sensed by the differences in the phase measurements of the four quadrants of the QPDs. A small tip or tilt motion of a TM caused not only a displacement of the respective measurement beam on the QPD ("beam walk"), but also an angle between the wave fronts. The former effect gives wide-range, but less sensitive, so-called differential power sensing (DPS) signals used for alignment and diagnostic purposes, while the latter produces phase shifts between the split segments of the QPDs and was used for accurate alignment sensing by the DWS [27,28] method. While it is possible to suppress the beam walk with imaging optics, this was not necessary in LPF due to the small expected TM angles. Not suppressing the beamwalk also enabled the use of the DPS signals for initial alignment of the TMs from conditions that could potentially be so strongly misaligned that the interferometers have no contrast and hence no usable DWS signal.

The X1 and X12 interferometers that sensed the TM motions and rotations used non-normal incidence

reflections off the TM surface at an angle of 4.5° to separate the returning beam. This was chosen because at the time of the design (2002) it was not clear whether normal incidence with beam separation by polarizing optics would be able to deliver the required $\mathrm{pm}/\sqrt{\mathrm{Hz}}$ stability at mHz frequencies. In the meantime such doubts have been resolved with laboratory measurements [29] such that future designs might use normal incidence.

The QPDs were connected to two hot-redundant phasemeter (PM) units, one of which processed all "A" QPDs and the other one all "B" diodes, such that in case of a failure of one photodiode or one phasemeter all signals were still available. In normal operation all channels were used. To implement the so called "balanced detection" two complementary QPD segments, one from each output port, were subtracted. This achieves better signal-to-noise ratio (SNR) and suppression of some noise sources [in particular laser relative intensity noise (RIN)]. Each phasemeter processed 16 channels in parallel, each consisting of an op-amp based transimpedance amplifier, followed by an antialiasing filter with 20 kHz bandwidth and a 16-bit successive-approximation analog to digital convertor (ADC) sampling at 50 kHz, with a clock driven from the DMU. The low value of $f_{\mathrm{het}} = 1$ kHz allowed moving all electronics and their associated heat dissipation away from the OB (in contrast to the interferometers in LISA, where MHz heterodyne frequencies require transimpedance amplifiers immediately adjacent to the photodiodes on the OB). Within the phasemeter, the digitized photocurrents or voltages, U_i, were further processed by a field programmable gate array (FPGA) that performed a single-bin discrete Fourier transform (SBDFT) [24]. For each segment of $N_{\mathrm{FFT}} = 500$ samples (10 ms and thus 10 cycles at 1 kHz), it computed the three quantities

$$y_{\mathrm{DC}} = \frac{1}{N_{\mathrm{FFT}}} \sum_{i=0}^{N_{\mathrm{FFT}}-1} U_i, \tag{1}$$

$$y_{\mathrm{Re}} = \frac{2}{N_{\mathrm{FFT}}} \sum_{i=0}^{N_{\mathrm{FFT}}-1} U_i \cos(\omega_{\mathrm{het}} t_i), \tag{2}$$

$$y_{\mathrm{Im}} = \frac{2}{N_{\mathrm{FFT}}} \sum_{i=0}^{N_{\mathrm{FFT}}-1} U_i \sin(\omega_{\mathrm{het}} t_i), \tag{3}$$

and auxiliary diagnostic quantities (the actual processing was using unsigned integer arithmetic). These were transmitted to the DMU at a rate of 100 Hz through a payload-wide Mil-bus.

Within the DMU, phases were determined by computing $\arctan(y_{\mathrm{Im}}/y_{\mathrm{Re}})$, followed by a phase-tracking algorithm to remove jumps of 2π; further signal combinations were formed to derive the DWS signals. With error handling and calibration, the processing was in reality more complex, and details can be found in [30]. The measurements were scaled to optical path lengths using the factor $\lambda/(2\pi)$, or equivalently to TM motion using the factor $\lambda/(2\pi)/(2\cos(4.5°))$, and to TM angles using calibration factors from electrical to optical phase of order 5000 $\mathrm{rad_{el.}}/\mathrm{rad_{opt.}}$, which were determined on ground [see Eq. (19)]. The measurements were then downsampled to 10 Hz and transmitted to the spacecraft computer for use in the DFACS system and as science data telemetered to Earth.

C. Development and prototyping

First proof-of-principle prototypes of the interferometer and phasemeter were built at the AEI in Hannover and at the University of Glasgow starting in 2002. An engineering model (EM) of the optical bench was completed in 2004 by Rutherford Appleton Laboratories and the University of Glasgow [31]. Around the same time, advanced prototypes of the phasemeter and AOM driving electronics were built in Hannover.

Interferometer noise performance meeting the requirements was first demonstrated in 2004 on an early optical test bed with fixed mirrors in place of the TMs [11,32]. Detailed noise investigations in Glasgow identified an important noise source named Small Vector Noise (SVN). It originates from electrical sidebands introduced by the Radio Frequency (RF) signals driving the AOMs which then convert into optical sidebands. These sidebands, in turn, result in a spurious interferometric signal in conjunction with fluctuations of the differential path length between the two fibers that deliver the light to the OB. [33]. A mitigation strategy of stabilizing the OPD between the two fibers using the phase measured in the reference interferometer as the error signal was experimentally demonstrated. Investigations in Hannover developed a firm theoretical understanding of this noise source. Two separate mitigation measures were subsequently introduced to the flight model requirements which led to a suppression of that noise to a negligible level. They consisted of placing very strict requirements on the spectral purity of the AOM driving frequencies and of implementing active stabilization of the OPD using a piezo behind the AOMs as actuators. Furthermore, the importance of laser RIN near the heterodyne frequency and its second harmonic was identified [34] and mitigated with an analog amplitude stabilization loop using dedicated power detection photodiodes on the OB (PDA1 and PDA2 in Fig. 2) as error signal and the RF amplitudes that drive the AOMs as actuators.

On the processing side, an analytically predictable phase error in the SBDFT-derived phase was found in the case of non-negligible phase shift occurring during one time segment (10 ms). If the changes are fast enough, they produce an equivalent frequency shift of the heterodyne signal. Since the SBDFT is always evaluated at the fixed heterodyne bin, sufficiently fast signals drift measurably out of

this bin, resulting in a nonsymmetric Fourier transform. We call this effect "Doppler error". It depends on the injection frequency and its offset to the heterodyne frequency for a given Fourier bin width. This error was mitigated by analytical correction formulas in the processing back end for the prototype measurements but was not visible under nominal in-flight operating conditions due to the achieved phase stability.

Prototypes of the data processing chain were developed in the laboratory [35] and served as model for the DMU software. It was also shown that angular jitter of the fixed "test mass" mirrors could be subtracted from the x_1 and x_{12} measurements [36], something which was also required in flight (see discussion in [12,37]).

Since each TM was contained in a separate vacuum enclosure, the measurement beams were transmitted through an optical window [38,39] mounted in the TM enclosure. The windows were 6 mm thick and made from the special glass S-PHM52 from Ohara, which was chosen for its small value of the total temperature-driven pathlength sensitivity, $dn/dT + (n-1)\alpha \approx 0.59$ ppm/K. They were coated with a conductive indium tin oxide (ITO) layer on the side facing the TM to avoid electrostatic disturbances due to charge accumulation on the otherwise isolating glass.

D. Flight hardware construction

The flight model (FM) of the OB was built in Glasgow between August of 2009 and March 2010 using hydroxy-catalysis bonding, a coordinate measurement machine and calibrated quadrant photodiode pairs to determine beam positions and directions in space with an accuracy of a few μm [40–42].

The laser beams were required to be well aligned to the center of mass of the TMs to minimize the coupling between SC rotation and apparent TM separation changes [tilt-to-length (TTL) coupling]. The alignment was measured prior to launch relative to the OB mechanical frame, i.e., relative to a virtual point against which also the electrode housing was aligned during assembly. For this, the ultimate alignment accuracy for the reflection point on the TM was found to be $\mathrm{TM1}_{\mathrm{offset}} = (-6, -15)$ μm and $\mathrm{TM2}_{\mathrm{offset}} = (-16, -7)$ μm, in the horizontal and vertical direction, which was comfortably better than the corresponding requirement of ± 25 μm for each value. The path length mismatches in the interferometers were controlled to better than 0.5 mm, well within the 1.0 mm requirement [43].

The beam splitters were rectangular cuboids of dimension (h/w/d) $20 \times 15 \times 7$ mm made from fused silica coated with appropriate dielectric coatings on both sides [44]. The recombination beam splitters have dimension of $20 \times 20 \times 7$ mm. The fiber collimators were quasimonolithic constructions made from rectangular fused silica pieces and an aspherical lens of focal length 6.24 mm [45,46], followed by a cubical polarizing beam splitter mounted under a small angle in order to clean the polarization of the beams before they enter the interferometer. The optical components were mounted on the baseplate of dimension $200 \times 212 \times 45$ mm made from Expansion Class 0 Zerodur which had an arched lower surface for mass reduction and had a mass of approximately 4.23 kg [47].

The FMs of the phasemeter were built by the University of Birmingham [48]. Initial processing took places in Actel (now Microsemi) FPGAs. The DMU was built in Spain and its design was led by the Institut d'Estudis Espacials de Catalunya [49,50].

The beam modulation unit ("laser modulator" in Fig. 2) was jointly built by Kayser-Threde, Contraves, and APC Paris and uses AOMs from Gooch and Housego in shear mode for reduced RF power consumption, lever-arm amplified piezo actuators for the OPD control and dedicated electronics from Contraves.

The laser was made by Tesat and delivered approximately 35 mW nominally at a single-mode, polarization maintaining fiber output. It had both a slow temperature input and a fast piezo input for laser frequency control, both of which were driven by signals from a digital control loop running in the DMU with a designed unity gain frequency of 240 mHz [51]. This control loop, which is separate from the beam modulation unit as shown in Fig. 2, used the phase measured in the Frequency interferometer as an error signal. A similar digital control loop also running in the DMU stabilized the OPDs with a designed unity gain frequency of 3.1 Hz [51].

The resulting optical power in each instance of the four measurement and reference beams that reached the photodiodes was approximately 1.2 mW. The power reflected from the TMs was around 2.4 mW for TM1 and around 1.2 mW for TM2, which is important for calculation of the TM forces from radiation pressure and its possible fluctuations.

After complete assembly of all interferometer elements in the spacecraft, numerous tests were performed [22,52], the most relevant one for this discussion being a thermal vacuum test performed at Industrieanlagen-Betriebsgesellschaft mbH (IABG) in Ottobrunn for three weeks in 2011, which verified the functional and noise performance with fixed mirrors substituting the TMs in a representative thermal environment.

E. Dedicated data-analysis framework

To analyze the data from the LISA Pathfinder mission, the object-oriented MATLAB© toolbox LTPDA has been developed and extensively tested [53]. Its key feature is to store data inside a so-called analysis object which keeps track of the operations that have been applied to it and creates an object history, providing full reproducibility of the results. It was adapted to the mission in two ways; first, the software allowed us to produce results fast enough to plan the following experiments on LISA Pathfinder while

remaining flexible enough to account for last-minute changes in the experiment and analysis designs, and second, it provided routines adapted to the LISA Pathfinder experiments which were developed before launch and tested on laboratory data. The results and figures presented in the following have all been generated using LTPDA.

III. IN-ORBIT PERFORMANCE

The OMS exhibited exceptionally stable performance throughout the mission with $32.0^{+2.4}_{-1.7}$ fm/$\sqrt{\text{Hz}}$ sensitivity above 200 Hz along x (as presented in [1]), substantially better than its requirement.

In this section we discuss the OMS in-orbit behavior in terms of its sensitivity and reliability in more detail. We show the performance under different operating conditions and also present our understanding of the contributing noise terms for both the longitudinal and the angular measurements.

The interferometer was first turned on during commissioning (13th January 2016) with still caged TMs and hence large misalignment. The propulsion module was also still attached to the SC at this time, resulting in a varying thermal environment under vibrational stress. Nevertheless, the OMS immediately demonstrated full functionality and noise levels well below 10 pm/$\sqrt{\text{Hz}}$ at a frequency range between (1 to 1000) mHz, despite having a contrast of only 0.6% in the X12 interferometer, limited by misalignment of the beams with the TMs in their "launch locked" positions.

The TMs were released during commissioning on 15./16.02.2016; a few days later they were aligned and dynamically controlled by DFACS using the interferometer signals. A contrast of around 99% in X12 and 98.5% in X1 was immediately achieved (see Fig. 4) and science operations started on March 1st, 2016.

Overall, the operational duty cycle of the OMS, measured in terms of laser and phasemeter functionality, between the start of science operations and July, 1st 2017 at 08:00 UTC reached 99.4%, demonstrating the system's reliability (see Sec. IV E).

One of the most important channels to be characterized in this publication is the differential TM to TM measurement, which is constructed onboard after taking the difference between the X12 and XR (reference) interferometer. We call this quantity

$$o_{12} \equiv -\kappa(x_{12} - x_{\text{R}}), \tag{4}$$

where $\kappa = \lambda/(4\pi\cos(4.5°))$ is used to calibrate to TM displacement (note the minus sign due to coordinate conventions).

We also present the X1 interferometer measurement

$$o_1 \equiv \kappa(x_1 - x_{\text{R}}) \tag{5}$$

in comparison, which is used for SC control.

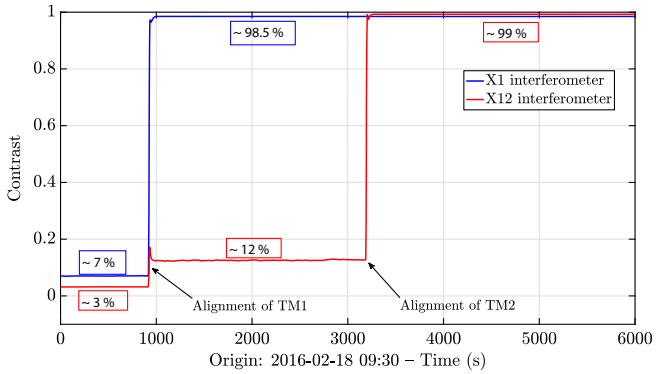

FIG. 4. Contrasts during TM alignment. The TMs were previously released and here aligned using electrostatic actuation, which improved the contrast considerably; best achieved in ground testing was ~93% using aligned mirrors. This behavior underlines the build quality of the OMS.

Without the κ factors, we call the quantities "raw" measurements; namely, $o_1^{\text{raw}}, o_{12}^{\text{raw}}$.

All the longitudinal signals are constructed using eight QPD segments. They are combined by applying balanced detection (subtracting complementary out-of-phase quadrants from the two output ports at the recombination beam splitter) and complex addition of the balanced segments.

We also characterize the angular measurements using DWS, for which pairs of balanced quadrants are subtracted (top and bottom, left and right), resulting in a slightly lower SNR compared to the longitudinal data.

As mentioned before, DWS uses calibration coefficients from ground measurements, that calibrate from the "raw" optical wave front phase difference to TM angle.

All the data processing takes place on-board, without the possibility to access individual photodiode quadrants during daily operations.

A. Typical spectra and comparison with ground measurements

In this section we look at some typical noise measurements of the longitudinal and angular measurements and compare to data from the ground test campaign.

1. Description of the data

The in-flight measurements for these examples were taken in March 2016 during the first two days of mission operations (2016-03-01 08:05—2016-03-03 00:00 UTC), just after the commissioning phase was completed.

The on-ground measurements were taken more than 4 years earlier during the on-station thermal tests (OSTT) campaign at IABG in Ottobrunn from October 26th, 2011—November 6th, 2011, during the hot (used for angular DWS data here) and cold (used for the longitudinal data here) test phase with temperatures of between approximately (9.5 to 30.5) °C.

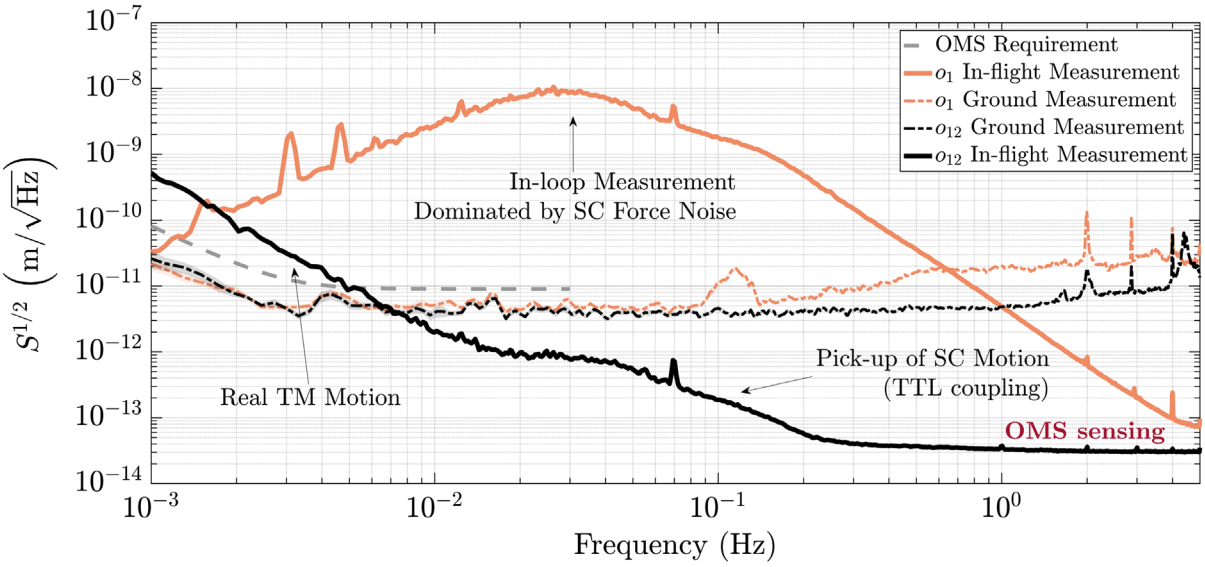

FIG. 5. Comparison of interferometric measurements of o_1 and o_{12} on-ground and in-flight. In the ground measurements, the noise in o_1 and o_{12} is comparable in the required measurement band. The in-flight measurement of o_{12} below about 200 mHz is dominated by cross-coupling from spacecraft jitter and real TM motion (see Sec. III C 2 and Fig. 12). At higher frequencies, the noise level is significantly below the ground measurements and OMS sensing noise is dominating (marked in red). The o_1 measurement in-flight is used to control the SC and as such represents an in-loop measurement, which is dominated by the force noise on the SC. This figure has been produced from a time series using the LPSD algorithm [54] with 66.1% overlapping BH92 windows [55], using as input parameters a desired 1000 Fourier frequencies with 100 averages.

The spectral densities of the longitudinal readouts o_{12} and o_1 are shown in Fig. 5, expressed as an amplitude spectral density (ASD). We give one measurement from on-ground tests and one from in-flight data, respectively, compared to the overall requirement of the OMS.

Similarly, Fig. 6 shows the corresponding DWS comparison.

2. Description of o_{12}

The in-flight o_{12} measurement of the relative x displacement of two TMs represents an "in-loop" sensor, used by DFACS to control the TM2 x electrostatic force to maintain constant TM separation. However, its unity gain frequency is around 1 mHz and has negligible effect on the data shown, especially the sensor noise dominated high frequencies.

We note that in general the sensing noise at those mHz frequencies cannot be measured but only estimated and bound by upper limits. As visible, the measured o_{12} displacement exceeds the optical metrology requirement at such frequencies less than 5 mHz, but this can most likely be attributed to true TM motion, since the sensor is designed to detect real distance fluctuations.

In addition, we provide measurements for mechanically fixed TMs by the Gravitational Reference Sensor (GRS) "grabbing positioning release" system during flight. These are shown along x in Figs. 17 and 18, while the angular DWS is presented in Fig. 19. This data suggest that also the in-flight noise at frequencies as low as 1 mHz is consistent with the level observed at higher frequencies.

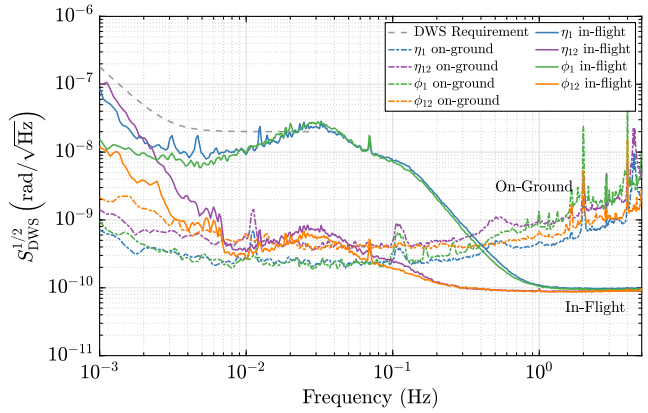

FIG. 6. Comparison of interferometric measurements on-ground and in-flight of the angular DWS TM readouts together with the noise requirement. The spectral shape is similar to the longitudinal measurements but has contributions from real TM movements (independently validated by low frequency (<mHz) capacitive sensing), SC jitter, star-tracker noise and OMS sensing noise. The latter is computed from the pseudoflat noise at high frequencies. This figure has been produced using the same LPSD algorithm as in Fig. 5.

For the data between (20 to 200) mHz we attribute the excess noise to pick-up of SC motion (TTL coupling), see Sec. III C 2 and [1,12,14].

As reported in the previous letter [1], the main o_{12} measurement recorded in-flight shows a quasiflat sensing noise floor at frequencies above 1 Hz which is much lower than on ground, at frequencies above 400 mHz up to more than a factor of one hundred.

The small peaks in the in-flight o_{12} data at 1 Hz, 2 Hz, 3 Hz, 4 Hz, and 5 Hz are probably due to electrical cross-coupling from the pulse-per-second timing signal present on the SC.

3. Description of o_1

The o_1 measurement shows a different spectral shape than the ground measurement. To explain this difference we consider that the o_1 measurement is also an in-loop measurement of another DFACS's drag-free control loop. This loop, with unity gain frequency of about 0.2 Hz, ensures that the SC follows the x position of TM1. It has a higher unity gain frequency than the control loop which uses o_{12}. Consequently, the o_1 spectral density is dominated by force noise of the SC, which originates mainly from the thrusters, and the gain of the drag-free control loop which suppresses this noise [17].

The lines around 1.5 mHz and its multiples, and probably the feature around 70 mHz as well, are associated to the thrusters [15]. This idea is also supported by the discussion in [56]. When comparing the amplitude of this feature in o_1 and o_{12}, we find that the ratio of the two amplitudes is slightly higher than what we could attribute to common-mode rejection [14]. However, the feature around 70 mHz is also observed by a capacitive position sensor of TM1 (not shown here, for details about this sensor, we refer to [57]). This is also confirmed during a period when the OMS served as an out-of-loop sensor, while the control was switched to the independent but less sensitive capacitive sensing. Another important test was performed during disturbance reduction system (DRS) operations, when the main cold gas thrusters were in standby mode, while another set of thrusters was used to control the SC [56]. We find that the interferometric readouts show no feature at 70 mHz for two selected and comparable timespans. Consequently, a platform jitter originating from the cold gas thrusters is a more likely reason, and the OMS does not cause this artifact.

4. Description of DWS measurements

The angular DWS measurements, presented in Fig. 6, have very similar characteristics towards frequencies above 1 Hz. The low frequency behavior has been analyzed in [17] and shows a combination of star tracker noise, TM torque noise, capacitive sensing noises, and SC force noise, since DWS has been used as an in-loop sensor for the DFACS. As can be expected by design, the differential channels show more than an order of magnitude common-mode rejection of those contributions.

We find that the high-frequency sensitivity, limited by the OMS, reached even below 100 prad/$\sqrt{\text{Hz}}$ during the mission, more than a factor of 200 better than required.

The ground measurements show comparable characteristics to the longitudinal data but had ample margin to their requirement.

5. Comment on the difference between ground and in-flight measurements

The results of the on-ground test campaign reported in [52], visible in Fig. 5, showed a measured performance of around $(3\,\text{to}\,8)$ pm/$\sqrt{\text{Hz}}$ around 10 mHz, a significantly higher noise level than observed during science operations.

During the ground tests, Earth's gravity did not allow for free-falling TMs under DFACS control as in-flight. Therefore, the TMs were replaced with fixed mirrors whose attitude and longitudinal position were hand-aligned. The alignment resulted in a somewhat nonoptimal phase offset between X12 and the reference interferometer, and a typically lower contrast than what was achieved in flight, resulting in some of the noise contributions being higher than in flight conditions.

However, this does not explain all of the extra noise.

The reason may be that the two separated mirrors, rigidly connected via individual piezoelectric transducers (PZTs), may not have been strictly stable to pm level. These individual mounts may also explain the difference between the o_1 and o_{12} noise levels above 30 mHz because of possible acoustic or seismic couplings that could cancel to some extent in the differential measurement. The origin of the feature in o_1 just above 100 mHz is discussed in more detail in [58]. However, the on-ground noise spectrum was never fully explained. Since the performance had been below the requirements, further investigations were not given high priority.

As we show in this article, the in-flight noise spectrum is well modeled (see the discussion below).

We present our noise model in Sec. III B and apply it to selected in-flight data under various conditions in Sec. III D. A complete mission overview is given afterwards in Sec. III F.

B. Noise model

Here, we summarize the noise model and sensing noise sources.

We extend our previously published description (see [1]) to include DWS measurements and the so called SVN that is minimized by the OPD. We also expand on indirect contributors like TTL and Brownian force noise and give more details on the two observed frequency noise states of the laser.

Our understanding of the system explains most of the sensing noise as a combination of noise sources associated with the laser (frequency and intensity noise), and noise sources associated with the phase measurement system (quantization noise, electronic noise).

Here, the focus is on the calibrated TM readouts of the X12 and X1 interferometer, which are computed on-board during the mission. Their sensitivity can best be modeled using data from all four interferometers. However, limitations apply as to how well we can model the data given the available measurements, see Sec. III E.

The total phasemeter noise is a combination of the noise introduced by both the analog and the digital stage. The noise in the analog part of the phasemeter is proportional to the equivalent input current noise noise of the ADCs and the electronic circuits and the noise in the digital part arises mainly from the quantization noise of the ADC converters used. In flight we cannot differentiate between the electronic circuit noise and the ADC noise and use the resulting total phasemeter noise instead.

Under nominal operating conditions, the phasemeter readout noise is the dominating noise term, scaling reciprocally with contrast and beam powers. Much smaller is shot noise due to the mW powers arriving at the photodiodes, for which the phase error scales reciprocally with contrast and the square root of the beam powers. Still, with a decreasing contrast also the impact of shot noise increases, since the signal has lower amplitude.

In terms of the laser, we analyzed two other noise sources that can dominate the performance, depending on the conditions: Laser frequency noise, and laser intensity noise.

The contribution of laser intensity or power noise is described by the so called RIN coupling (see [34]). RIN at the heterodyne frequency couples directly into phase noise but is suppressed by the use of balanced detection and an analog power stabilization control loop (see Sec. II C).

At twice the heterodyne frequency, 2 kHz, the laser-power control loop has a smaller gain. There also exists a coupling mechanism, which is, however, phase matched with the signal and thus cannot be canceled by balanced detection. Instead, this coupling appears correlated on all interferometers and therefore depends on the phase difference between the corresponding combinations. For the longitudinal measurements it is the difference between the X1 or X12 and the XR interferometer and for the angular readout via DWS it is the difference of the involved quadrants.

Accordingly, this noise source is minimized if the phase difference is around zero radian and thus contributes very little if the TMs are at the nominal longitudinal positions (close to zero offset). However, angular offsets were introduced during the mission to mitigate TTL coupling that in turn let to an increase of the RIN contribution.

Furthermore, low frequency RIN couples as a direct force noise on the TMs via radiation pressure to the phase readout. This is suppressed by the power control loop.

The optical components are also affected by thermally driven effects, which have been explained in more detail in [1]. We apply the same upper limit on these path length noises in the noise budget plots given here.

In the following we analyze two noise sources in greater detail that have not been (fully) covered in [1].

1. Laser frequency fluctuations

Frequency fluctuations $\delta\nu$ of the laser introduce a phase error $\delta\varphi$ due to unequal optical path lengths ΔL between the interfering beams, as described by [1]

$$\delta\varphi = 2\pi\frac{\Delta L}{c}\delta\nu. \tag{6}$$

c denotes the speed of light.

In a first processing step aboard LPF, the measurement of the reference interferometer, x_{R}, is subtracted from that of the frequency interferometer, x_{F}. We define Ψ_{F} as this difference,

$$\Psi_{\mathrm{F}} = x_{\mathrm{F}} - x_{\mathrm{R}}. \tag{7}$$

A dedicated control loop used Ψ_{F} as an in-loop sensor to reduce this noise [24].

The coupling of the remaining frequency fluctuations to the longitudinal readouts is dictated by the difference in optical path length between the measurement and the reference beam, as described by Eq. (6). In the case of the LPF o_1 and o_{12} measurements, we have to take the subtraction of the reference interferometer into account, so that the difference in path length difference between the respective interferometer and the reference interferometer determines the amount of coupling.

This quantity was found to be subject to small changes in the course of the mission, due to the absolute positioning of the two TMs. From dedicated laser frequency modulation experiments, the path length mismatch $\Delta L_{12} - \Delta L_R$ was estimated to be around 368 μm in June 2016 and around 329 μm in January 2017 [59]. These values have been used to obtain the respective frequency noise contributions in Sec. III D.

During the mission, we experienced periods of increased laser frequency noise which resulted in an increase of the total noise in o_{12} (see Sec. III F).

Due to telemetry limitations, not the full frequency noise data was available throughout the mission. However, we still have reason to believe that our frequency noise estimation is consistent. We see that its subtraction from the o_{12} measurement removes the periods of increased noise, as shown in Fig. 7. For clarity, we have band passed the data from (0.2 to 1.9) Hz. The coupling coefficient $H_{o_{12}}$ has been estimated from the transfer function during the periods of increased laser frequency shown and is consistent with the results.

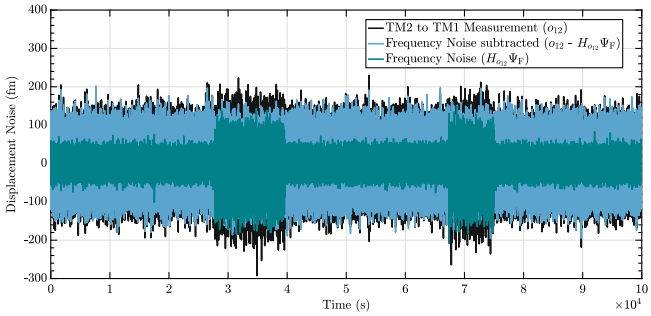

FIG. 7. Band-passed data (starting on 2016-03-01 08:05 UTC) for Ψ_F, o_{12} and o_{12} with the laser frequency noise contribution subtracted. We can see that this subtraction removes periods of increased noise in o_{12}. It supports the idea that frequency noise is responsible for the multimodal noise behavior of o_{12}, visible in Fig. 20. Based on Fig. (7.2) in [59].

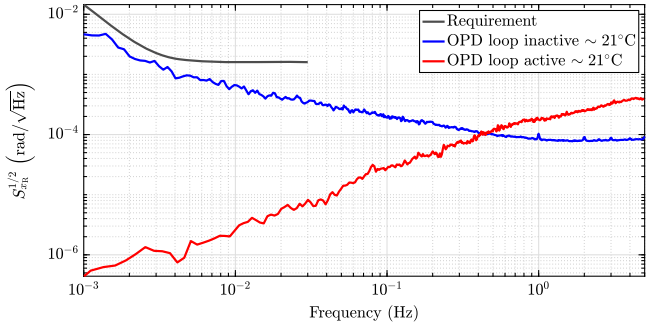

FIG. 8. Two examples of the ASD of the reference interferometer measurement x_R (in-loop measurement) when the OPD control loop was inactive and when it was operating as measured in-flight. The requirement is based on the significant SVN coupling measured during ground tests, see Sec. II C.

Unfortunately, this verification could only be done for the first noise runs since in the subsequent noise measurements the laser frequency noise was either not telemetered at 10 Hz or no period of increased noise was occurring in the respective noise run. However, we have found no reason to assume a different behavior at other times, given that we continue to observe periods of increased noise in the two channels at the same time over the course of the mission, and the 1 Hz data indicates an increased spectral noise power.

This contribution is also visible in the noise budget for a similar period in Sec. III D 2.

2. *Small vector noise (SVN)*

As explained in Sec. II C, SVN originating from electric crosstalk between the two modulation frequencies of the AOMs was mitigated by design in two ways: via a stringent requirement on the spectral purity of the AOM driving frequencies and via the OPD control loop. In this paragraph, we will look at the remaining level of SVN in-flight. This analysis was not yet included in [1].

For characterizing the suppression of SVN we deliberately applied triangular path length differences through the OPD actuators. This appears in the x_R measurement, which, under nominal operating conditions, is used as an in-loop measurement of the OPD control loop.

In general, in-flight, the path length difference fluctuations in the fibers were below the requirement, see Fig. 8. The in-flight data shown here is from 2016-06-11/12 (inactive loop) and 2016-06-02 (active loop). The OB temperature sensors report temperatures around 21°C for the two periods of in-flight data.

The blue trace in this figure is the ASD of the reference interferometer measurement x_R when the OPD loop was inactive. The level of fluctuations is most likely due to a relatively stable thermal environment of the SC. This was not the case for the on-ground measurements.

With an activated OPD control loop the noise in x_R is comparable to the example shown in red in Fig. 8.

By comparing these two measurements, we find that the control loop suppresses the noise at frequencies below 0.4 Hz and increases the noise above this frequency. We believe the OPD actuator is adding noise at high frequencies but the details are still under investigation, see also [60].

We observed that the piezo-controlled loop exhibits spikes at around its actuation frequency of 100 Hz which are aliased down to lower frequencies. This OPD actuator contributes its own noise and often leads to increased noise towards the end of the 10 Hz spectrum.

The related discrepancy to the designed unity gain frequency was already noted before launch and was attributed either to a change in noise level between different measurement times or a different control loop response when operated under fully closed-loop conditions [61].

In addition, a few dedicated OPD loop characterization experiments are under study. Nonetheless, the requirement on the noise in x_R is fulfilled and the SVN contribution is minimized. To measure the remaining SVN sideband strengths directly, a set of experiments that deliberately amplified this coupling have been performed and analyzed. The impact of SVN was modeled following [33]. For a given OPD injection at frequency f_{inj}, this model considers two small contributing vectors; one at the frequency $(1f_{inj})$ and one at twice the frequency $(2f_{inj})$.

Like any other vector noise the magnitude of the coupling depends on the differential phase when subtracting correlated measurements and behaves therefore similar to RIN.

For o_{12}^{raw} the model reads in the time domain

$$N_{X12,SVN} = \left(k_1 \sin\left(\frac{x_R + x_{12}}{2}\right) + k_2 \cos\left(\frac{x_R + x_{12}}{2}\right)\right) \sin\left(\frac{o_{12}^{raw}}{2}\right) + \left(k_3 \sin\left(x_R + x_{12}\right) + k_4 \cos\left(x_R + x_{12}\right)\right) \sin(o_{12}^{raw}). \quad (8)$$

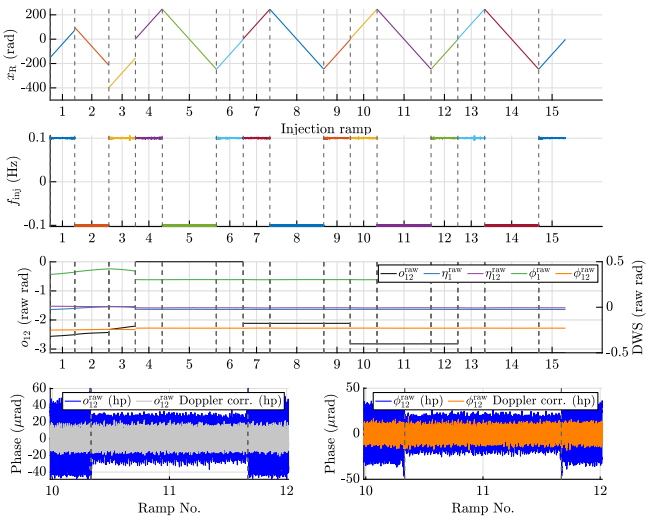

FIG. 9. SVN experiments during the mission. The top panel shows the phase ramp injections through the OPD, next we display the stable injection frequencies and the raw offset of the readouts, since those control the strength of the coupling. The last row shows the effect of the Doppler correction on the data with an exemplary zoom on ramp 11 (with high pass). The data stems from January (before cooldown) and February 2017 (during cooldown). One ramp was in the order of 5–10 minutes.

The in-flight experiments aim at estimating the sideband strengths k_i.

These experiments are detailed in Fig. 9. "Fast" phase ramps were injected through the OPD loop and resulted in sinusoidal phase noise in the raw phase signals.

One experiment took place before, and one during the cooldown of the SC in the beginning of 2017.

When analyzing this experiment, we had to correct for the "Doppler error", due to the fast phase changes (see Sec. II C).

We were able to calculate and remove this effect, that leads to wrong amplitude estimates, see also the bottom panels of Fig. 9 and [33]. It was calculated specifically for the flight phasemeter and estimated based on the limited telemetry.

However, the Doppler error is not relevant in nominal operations, when the phase changes are much slower.

From fitting the SVN noise model to these injections in all channels with appropriate SNR, we found a similar set of coupling vector amplitudes for the different operating conditions, while likely only their phase relation changes.

The main findings are that the 1f-SVN contributions are below $|2\ \mu\text{rad}|$, while the 2f-SVN coefficients reach almost $|40\ \mu\text{rad}|$, see Fig. 10.

These sidebands are further minimized by the sin() of the differential phase during the mission, because the nominal offsets are almost zero for o_{12}. For the rotational degrees-of-freedom the contributions are slightly higher due to the DWS alignments.

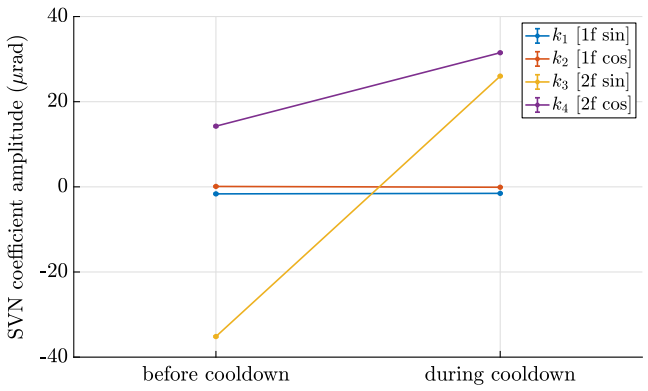

FIG. 10. Averaged SVN coefficient fit results before (ramps 1–3) and during cooldown (ramps 4–15). These are the only ramp injections during the nominal mission, so for most of the time we apply the "before cooldown" coefficients to estimate the SVN contribution. We suspect a phase rotation during cooldown in the k_3 coefficient—the total sideband strength remains approximately the same.

For example, with an o_{12} offset of 10 nm we estimate a contribution of around 0.1 fm/$\sqrt{\text{Hz}}$ at 1 Hz.

Overall, the measurements and experiments confirm that SVN was well mitigated.

3. Summary of the longitudinal noise model

To summarize, our noise model for the noise power in units of power spectral density (PSD) consists of the uncorrelated sum of:

(i) X12 phasemeter noises (shot noise, ADC noise and electronic noise that depend reciprocally on the X12 contrast and power).
(ii) XR phasemeter noises (shot noise, ADC noise and electronic noise that depend reciprocally on the XR contrast and power).
(iii) XF frequency noise to o_{12} coupling.
(iv) RIN to o_{12} coupling.
(v) SVN to o_{12} coupling.
(vi) Thermally driven noise on the OB as a conservative upper limit neglecting common-mode effects, see [1] for more details.
(vii) (Not from the sensor: Indirect contributions).

The same holds true for the X1 interferometer by adjusting the inputs accordingly. Detailed equations were given in [1].

4. Description of the angular noise model

The angular noise model is similar to the longitudinal cases. Differences arise from the different calibration factors, the missing subtraction of the XR interferometer readout, the good suppression of frequency noise and the different channel combinations. We give the exact coupling formulas here, since they have not been published yet.

The parameters are described in detail in [1]. In short we have the contrast C, the elementary charge e, the normalized average total power per interferometer Σ, the voltage range of the ADC, U_{ADC}, and the effective transimpedance R_{TIA}.

For DWS readout $\gamma \in \{\phi_1, \phi_{12}, \eta_1, \eta_{12}\}$ in a corresponding interferometer $K \in \{\mathrm{X12}, \mathrm{X1}\}$ we find the shot noise

$$S^{1/2}_{K,\mathrm{shot,DWS}} = \frac{4}{C_K}\sqrt{\frac{e}{2\Sigma_K \frac{U_{\mathrm{ADC}}}{R_{\mathrm{TIA}}}}}, \tag{9}$$

and the phasemeter noise (labeled "PM", $S^{1/2}_{I_{\mathrm{tot}}}$ describes the noise current produced by electronics and ADCs)

$$S^{1/2}_{K,\mathrm{PM,DWS}} = \frac{8S^{1/2}_{I_{\mathrm{tot}}}}{2C_K\Sigma_K \frac{U_{\mathrm{ADC}}}{R_{\mathrm{TIA}}}}. \tag{10}$$

The level of RIN at twice the heterodyne frequency is described by the power fluctuations over its mean power (at that frequency), expressed as an ASD called r, and contributes a phase error given by

$$S^{1/2}_{\gamma^{\mathrm{raw}},\mathrm{RIN}} = \sqrt{2}r|\sin(\gamma^{\mathrm{raw}})|. \tag{11}$$

Here, γ^{raw} is the uncalibrated phase of the electrical current in units of radian (i.e., representing wave front differences).

The coupling N_{SVN} of SVN to the phase readout is modeled by a linear combination of the corresponding sidebands with strengths k_i as described above, adjusted and estimated for DWS given the available data,

$$\begin{aligned} N_{K,\gamma^{\mathrm{raw}},\mathrm{SVN}} = {} & (k_1\sin(x_K) + k_2\cos(x_K))\sin(\gamma^{\mathrm{raw}}/2) \\ & + (k_3\sin(2x_K) + k_4\cos(2x_K))\sin(\gamma^{\mathrm{raw}}). \end{aligned} \tag{12}$$

Note that the longitudinal measurements x_K that enter the equation above are used to approximate the unavailable quadrant phase data.

These sidebands have been estimated to be below $|k_i| < 40\ \mu$rad by the dedicated experiments discussed before. We call the resulting noise power $S_{K,\gamma^{\mathrm{raw}},\mathrm{SVN}}$.

The total noise model for each DWS channel is a combination that reflects the data processing with the calibration factors g_i (inverse of $\mathrm{rad_{el.}}/\mathrm{rad_{opt.}}$ from Sec. II B),

$$g_1 = (-0.202 \pm 0.004) \times 10^{-3}\ \mathrm{rad/rad}, \tag{13}$$

$$g_2 = (0.209 \pm 0.004) \times 10^{-3}\ \mathrm{rad/rad}, \tag{14}$$

$$g_3 = (-0.175 \pm 0.006) \times 10^{-3}\ \mathrm{rad/rad}, \tag{15}$$

$$g_4 = (-0.189 \pm 0.003) \times 10^{-3}\ \mathrm{rad/rad}, \tag{16}$$

$$g_5 = (0.188 \pm 0.007) \times 10^{-3}\ \mathrm{rad/rad}, \tag{17}$$

$$g_6 = (-0.193 \pm 0.004) \times 10^{-3}\ \mathrm{rad/rad}, \tag{18}$$

with the uncertainties originating from on-ground calibration measurements with approximately 2% errors, recalculated for the in-flight coefficients.

These are applied in the following way:

$$\phi_1 = g_1\phi_1^{\mathrm{raw}}, \tag{19}$$

$$\eta_1 = g_2\eta_1^{\mathrm{raw}}, \tag{20}$$

$$\phi_2 = g_3\phi_1^{\mathrm{raw}} + g_4\phi_{12}^{\mathrm{raw}}, \tag{21}$$

$$\eta_2 = g_5\eta_1^{\mathrm{raw}} + g_6\eta_{12}^{\mathrm{raw}}. \tag{22}$$

Therefore, the total model for DWS in the X1 interferometer reads as

$$\begin{aligned} S_{\phi_1} = {} & g_1^2(S_{\mathrm{X1,shot,DWS}} + S_{\mathrm{X1,PM,DWS}}) \\ & + g_1^2(S_{\phi_1^{\mathrm{raw}},\mathrm{RIN}} + S_{\mathrm{X1},\phi_1^{\mathrm{raw}},\mathrm{SVN}}), \end{aligned} \tag{23}$$

$$\begin{aligned} S_{\eta_1} = {} & g_2^2(S_{\mathrm{X1,shot,DWS}} + S_{\mathrm{X1,PM,DWS}}) \\ & + g_2^2(S_{\eta_1^{\mathrm{raw}},\mathrm{RIN}} + S_{\mathrm{X1},\eta_1^{\mathrm{raw}},\mathrm{SVN}}). \end{aligned} \tag{24}$$

The model for the calibrated X12 DWS is slightly more convoluted due to the linear combinations,

$$\begin{aligned} S_{\phi_{12}} = {} & (g_3 - g_1)^2(S_{\mathrm{X1,shot,DWS}} + S_{\mathrm{X1,PM,DWS}}) \\ & + g_4^2(S_{\mathrm{X12,shot,DWS}} + S_{\mathrm{X12,PM,DWS}}) \\ & + ((g_3 - g_1)S^{1/2}_{\phi_1^{\mathrm{raw}},\mathrm{RIN}} + g_4 S^{1/2}_{\phi_{12}^{\mathrm{raw}},\mathrm{RIN}})^2 \\ & + ((g_3 - g_1)S^{1/2}_{\mathrm{X1},\phi_1^{\mathrm{raw}},\mathrm{SVN}} + g_4 S^{1/2}_{\mathrm{X1},\phi_{12}^{\mathrm{raw}},\mathrm{SVN}})^2, \end{aligned} \tag{25}$$

$$\begin{aligned} S_{\eta_{12}} = {} & (g_5 - g_2)^2(S_{\mathrm{X1,shot,DWS}} + S_{\mathrm{X1,PM,DWS}}) \\ & + g_6^2(S_{\mathrm{X12,shot,DWS}} + S_{\mathrm{X12,PM,DWS}}) \\ & + ((g_5 - g_2)S^{1/2}_{\eta_1^{\mathrm{raw}},\mathrm{RIN}} + g_6 S^{1/2}_{\eta_{12}^{\mathrm{raw}},\mathrm{RIN}})^2 \\ & + ((g_5 - g_2)S^{1/2}_{\mathrm{X1},\eta_1^{\mathrm{raw}},\mathrm{SVN}} + g_6 S^{1/2}_{\mathrm{X1},\eta_{12}^{\mathrm{raw}},\mathrm{SVN}})^2. \end{aligned} \tag{26}$$

Note that the RIN and SVN here is a correlated quantity, meaning that the $|\cdot|$ operator on the sine in Eq. (11) is dropped in η_{12} and ϕ_{12}.

We include no thermally driven noise in DWS since we do not have independent investigations and modeling regarding its influence.

C. Indirect sensor noise contributions

1. Brownian noise

Brownian force noise is not a limiting noise of the sensor, but rather the cause of real, low frequency TM motion that

is detected by the optical readout. It is the most relevant source of TM acceleration noise in the mHz to 100 mHz regime and thus becomes the dominant noise at the frequencies, below roughly 60 mHz, where true TM motion is larger than sensing noise.

We include a simple model based on the estimation in [12] with a residual white differential TM acceleration noise of $S_{\mathrm{B}}^{1/2} = (5.2 \pm 0.1)\,\mathrm{fm\,s^{-2}}/\sqrt{\mathrm{Hz}}$ yielding an equivalent path length noise in early April 2016 (after integrating twice) of

$$S_{\mathrm{B,o12}}^{1/2} = \frac{S_{\mathrm{B}}^{1/2}}{(2\pi f)^2}. \tag{27}$$

The level of $S_{\mathrm{B}}^{1/2}$ decreased throughout the mission [13].

We note that this displacement noise is calculated at frequencies where control forces are not relevant.

For DWS, the TM torque noise is not solely dominated by the corresponding Brownian torque noise (which can be propagated from Δg by following [62]) and is therefore not included here due to the more complex control forces as analyzed in [17].

2. Angular and lateral motion cross-coupling (TTL noise)

The angular and lateral motion of the three bodies (TMs and SC) involved in the X1 and X12 interferometric readouts can leak into the longitudinal measurements through misalignments between the TMs and the optical system. We often refer to this noise as TTL coupling [63].

Since the motion of the SC can always be interpreted as TM motion with respect to the SC, we can describe this leakage by the effect of TM motion on the beam path only. In the case of angular jitter of either of the TMs, the measurement beam tilts due to the reflection at the respective TM. A rotation of the TM around an arbitrary point of rotation additionally moves the TM surface in or out of the beam path. Lateral TM jitter, i.e., motion along its y- or z-axis, couples into the interferometric readout via static angular misalignments of the TMs with respect to the optical system. A lateral shift of a tilted TM moves its reflective surface in or out of the measurement beam path, decreasing or increasing its path length.

In both cases, the reference beam remains unchanged under this motion. Therefore, the TM motion yields an altered optical path length difference, relative angle, and relative beam offset in the X1 interferometer for X1 motion and the X12 interferometer for motions of both TMs. All these effects will change the longitudinal readout.

Changes in the relative angle due to TM angular jitter are additionally visible in DWS of the respective interferometers. However, we expect the angular motion of the SC to cancel in the X12 DWS readout due to the nearly free-fall of the TMs: The angular jitter of the SC can be interpreted as a rotation of both test masses around the center of mass of the SC by the negative SC angle. Therefore, the beam tilts due to the reflection at both TMs. Since the tilt of the second TM affects the beam inversely compared to the first TM, the beam tilt is compensated by its reflection at TM2.

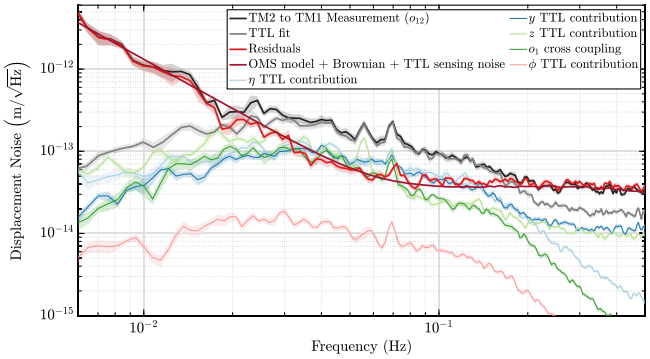

FIG. 11. The measurement data of a nominal run (same as presented in [1] and here in Fig. 12), corrected for the TTL contributions using a frequency domain fit. After the TTL subtraction, it becomes evident that the noise level of the corrected o_{12} extends down to approximately 90 mHz. However, due to the subtraction, sensing noise from multiple degrees of freedom is added to the OMS model estimate as visible at higher frequencies in the red curves, increasing the OMS noise compared to Fig. 12. Note that only 1 Hz data was available for y, z such that a downsampling filter reduces the visibility of the additional noise here. The raising spectral shape towards lower frequencies is consistent with the measured TM displacement due to Brownian force noise.

During the LPF mission, TTL noise has been reduced via realignments of the TMs. In particular, rotations to new nominal positions have reduced or counteracted TTL noise contributions [64]. The residual noise has been minimized by fitting and subtracting a linear model in postprocessing [14,37].

In most of the results presented here (such as Fig. 5), this coupling is not subtracted and is often visible as a "bump" of noise between (20 to 200) mHz. Figure 11 shows an example of the sensing noise after the subtraction of this effect. It has been modeled similar to the description in [14]. Here, however, we applied a fit in the displacement domain instead of acceleration, which was the usual method during the mission. The model uses a linear combination of translational and rotational displacement estimates of the SC and corresponding coupling coefficients. We also add a cross-coupling term for o_1 that describes the amount of remaining common-mode translational jitter in o_{12} due to imperfections in the setup.

The fit model reads

$$S_{\mathrm{TTL}} = a_{o_1} o_1 + a_\phi \bar{\phi} + a_\eta \bar{\eta} + a_y \bar{y} + a_z \bar{z}, \tag{28}$$

with the SC variables ϕ, η, y, z describing the motion relative to the differential TM measurement, calculated

from the (detrended) TM1 and TM2 readouts, e.g., $\bar{\phi} = (\phi_2 + \phi_1)/2$, and the coupling coefficiencts a_i.

The fit has been performed in frequency domain, using a iteratively reweighted least squares method in the range (22–100) mHz, avoiding the influence of frequency noise, and overlapping Blackman-Harris 92 windows with 24 averages.

Our fit result is consistent with the value given in [14], Table 1, for $\delta_{\mathrm{ifo},2}$ matching a_{o_1} for this time of the mission.

The capacitive sensors provide the y and z measurements; hence, their higher sensing noise increases the noise level in the data that has TTL contributions subtracted. Our ability to estimate this additional sensing noise is limited, however, and based on the fit result at high frequencies, which is filtered due to the onboard downsampling to 1 Hz. With higher sampled data available, the SC contributions could be low-pass filtered to reduce the additional noise towards higher frequencies where the TTL contribution is not limiting.

We do not attribute the TTL noise to the sensor itself since it does not depend on properties like beam characteristics or the measurement chain but can be described independently by SC motion. Subtracting it also adds sensing noise of the measurements of the contributing degrees of freedom. Further, not all the data channels needed for the subtraction were always available with a sampling frequency of 10 Hz. For these reasons, TTL has not been included in the OMS noise model in general.

Further details of the treatment of TTL in LPF can be found in [14,37]. For a detailed analysis of sources and physical origins we refer to [67,68].

D. Testing and validation of the sensing model

The performance observed during flight can be considered under various conditions that correspond to high, intermediate and low contrast. They give rise to different total noise levels in the X12 interferometer, both in terms of the longitudinal readout and the DWS signals. In the following, the same model of the underlying noise sources is used and shows good agreement with the measured noise.

The first condition (shown in Secs. III D 1 and III D 2) is where the alignment of the test masses is optimal. This condition is achieved in the nominal science mode. There, TM1 is in free-fall along the sensitive x-axis and TM2 is controlled to follow it in this degree of freedom. The angular orientation along ϕ and η of both TMs is controlled using the DWS signals. By choosing an appropriate working point of the DFACS controller the relative phase o_{12} of the X12 and reference interferometers is kept close to zero. In this condition, the extremely low noise of the X12 interferometer means that motion of the TM dominates any measurement below approximately 20 mHz. At higher frequencies, the measurement of the relative position of the two TMs is limited by the sensing noise in the X12 interferometer, which is dominated by a combination of RIN coupling at $2 \times f_{\mathrm{het}}$, ADC quantization noise, and frequency noise.

The second condition (shown in Secs. III D 3 and III D 4) corresponds to a medium-level contrast which was achieved by deliberately misaligning the TMs or by reducing one of the beam powers. Some of the noise contributions depend on the contrast. This gives us the possibility of examining the sensitivity of an interferometer as a function of contrast, and therefore of validating the intrinsic noise levels discussed above. Since the RIN (and SVN) coupling to o_{12} does not depend on the contrast but rather only on the TM position it is possible to disentangle contributions of correlated and uncorrelated noise sources.

The third condition under which we can study the interferometer performance is when the TMs are both mechanically grabbed (shown in Sec. III D 5). In this condition, the relative motion of the two TMs is restricted to that induced by thermomechanical fluctuations of the grabbing fingers that hold the test masses. In addition, the alignment of the two TMs (both in attitude and longitudinally) is far from optimal, with tens of micrometer and hundreds of microradian offsets. This nonoptimal alignment results in two effects; a nonzero phase offset between the X12 and reference interferometers, and a very low contrast (due to misalignment of the measurement beam's wave front with respect to the fixed wave front of the reference beam).

1. Noise budget under nominal conditions

Figure 12 shows an o_{12} measurement in nominal configuration. The noise contributions are estimated according to the noise model and show good agreement with the measurement.

This is one of the few occasions when the frequency interferometer data were transmitted to ground with 10 Hz sampling.

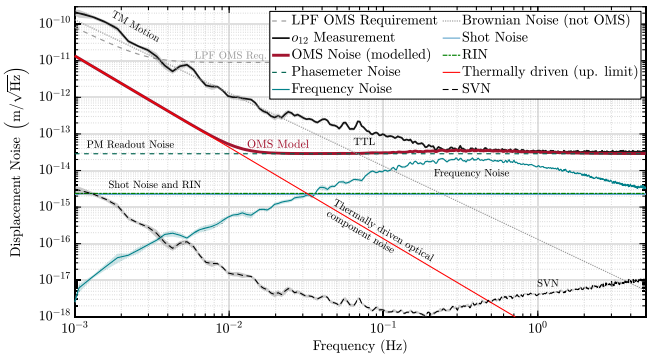

FIG. 12. Noise model applied to an o_{12} measurement from June 1st, 2016 starting at 18:46 UTC and lasting until 20:29 UTC in nominal configuration. Shown is the ASD computed with the same LPSD algorithm as in Fig. 5. Below 20 mHz TM motion caused by Brownian force noise dominates the noise spectrum. Modified from [1] by including SVN. We see that this noise contribution has negligible impact due to the implemented mitigation strategies.

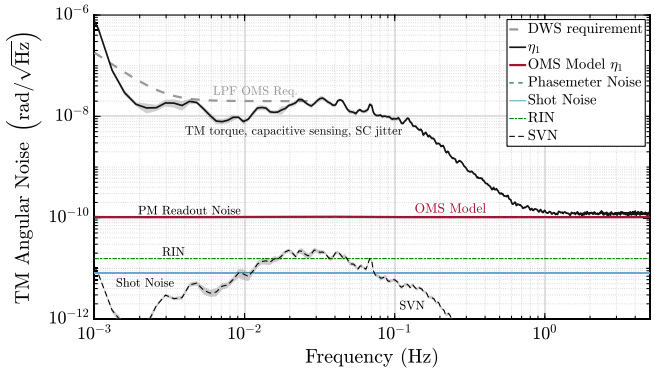

FIG. 13. Noise model and measurement of the η_1 DWS channel at the same time as Fig. 12. Between (0.001 to 1) Hz, the spectral shape results from a combination of angular noise from the star tracker, torque noise on TM1, capacitive sensing and SC force noise, as analyzed in [17]. The influence of the OMS is observed in the quasiflat sensing noise floor above 1 Hz only.

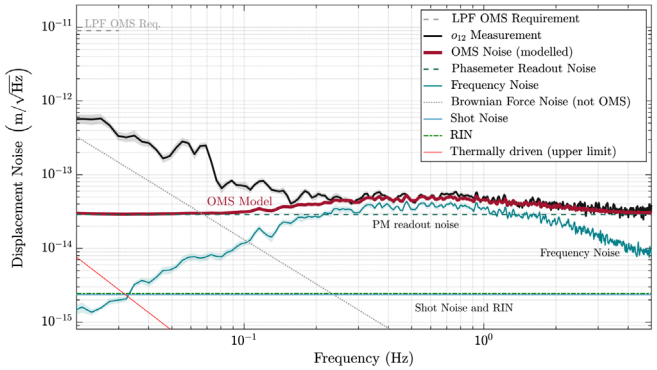

FIG. 14. Noise behavior for a higher frequency noise state; the model has been applied to an o_{12} measurement from January 2017. This measurement is comparable to Fig. 12. Here, however, a period of increased laser frequency noise is under study which is then the dominating noise source from approximately (0.1 to 1.5) Hz. Note that the SVN is not shown, since it is estimated to be below 1×10^{-17} m/$\sqrt{\text{Hz}}$.

Our model explains the measured noise density between (0.2 to 5) Hz. Between (20 to 200) mHz the measured noise is increased due to TTL coupling. We find that phasemeter noise (and within that, the ADC noise) is the dominating term in this condition.

Frequency noise causes the spectrum to increase slightly between (0.15 to 2) Hz. RIN and SVN coupling is highly suppressed due to the controlled TM position.

Below 20 mHz TM motion caused by Brownian force noise is detected. The estimate is based on the Δg measurement of April 2016 [13].

We find that the reference interferometer has almost the same noise levels in shot and phasemeter noise. This is expected due to its very similar design and parameters. Since the reference interferometer is subtracted, its noise adds to the combined readout o_{12}.

Figure 13 shows the sensitivity for DWS by example of η_1 for the same timespan as the nominal o_{12} budget plot given above.

The noise model includes the described noise sources, using the appropriate coupling factors for DWS signals. We find that the noise model has slightly larger deviations from the measurements in DWS compared to the longitudinal o_{12} data. This will also become visible later in Fig. 23.

We note that η_1 is an in-loop measurement of the DFACS with a unity gain frequency of around 1 mHz.

The pick-up from SC jitter as well as other force and torque noises is visible between (0.001 to 1) Hz, see [17], and therefore in a larger band compared to o_{12}.

2. Noise budget for o_{12} during a period of increased laser frequency noise

As explained in Sec. III B 1, we observed periods of increased laser frequency fluctuations during the LPF operations.

We show one example of the OMS noise model under these circumstances in Fig. 14.

During these periods, laser frequency noise becomes the dominating noise source in the o_{12} measurement in the frequency range from approximately (0.1 to 1.5) Hz.

This supports the previously stated hypothesis that the two levels of noise in o_{12} observed over the course of the mission (clearly visible in Sec. III F), are indeed due to an increase in laser frequency noise.

As anticipated in Sec. III B 1, this plot makes use of the path length mismatch $\Delta L_{12} - \Delta L_R \approx 329\ \mu$m, resulting from a dedicated experiment [59].

3. Noise behavior at intermediate contrasts

The data in Fig. 15 originates from an experiment in which both TMs were commanded to a range of angular tilts, which resulted in an overall reduced contrast due to imperfectly aligned wave fronts.

We selected stable timespans during which the measured noise floor has a flatness comparable to actual white noise.

The TM orientation also affects the RIN coupling effect to o_{12}, because a geometric piston couples TM tilt into the longitudinal path measurement of the X12 interferometer, causing the RIN coupling to vary depending on the piston crosstalk strength. The piston arises when the TM angles are controlled to certain offsets, because the rotation has its origin in the center of mass of the TM (and not at the point of reflection). This is visible in the fluctuations of the light blue RIN contribution in Fig. 15.

The resulting noise floor in o_{12} is estimated from a frequency average in the band (1.2 to 2.8) Hz (from PSD) as described in Fig. 20 and plotted over the X12 contrast.

We can see the influence of the contrast on shot and PM noise and the variation of the two frequency noise states, whereas RIN is only coupling via the longitudinal phase

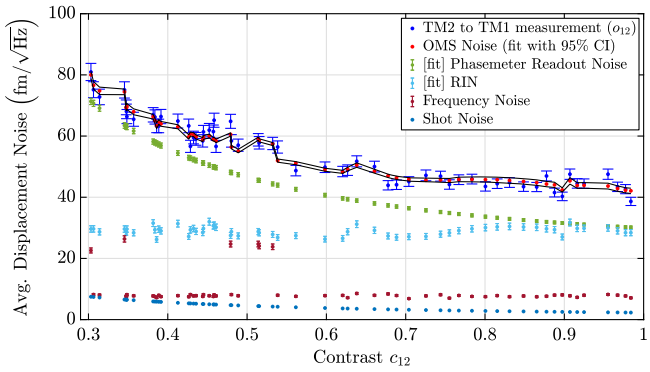

FIG. 15. Noise model at intermediate contrasts. For this figure we fitted the noise model as stated in [1] to an o_{12} measurement between (1.2 to 2.8) Hz with two free parameters (levels of RIN and ADC noise). The measurement is from a dedicated experiment (performed 2017-02-06 23:06:00 UTC—2017-02-08 22:55:00 UTC) in which the TMs were deliberately tilted. The TM orientation influences the RIN coupling strength and the interferometer contrast. Here, the fit yields RIN $r = (2.59 \pm 0.09) \times 10^{-6}/\sqrt{\text{Hz}}$ and ADC $S_{I_{\text{ADC}}}^{1/2} = (108.0 \pm 1.6)$ pA$/\sqrt{\text{Hz}}$. The SVN contribution is not shown, because it reaches only subfemtometer level. Overall, we find good agreement between the model and measurement.

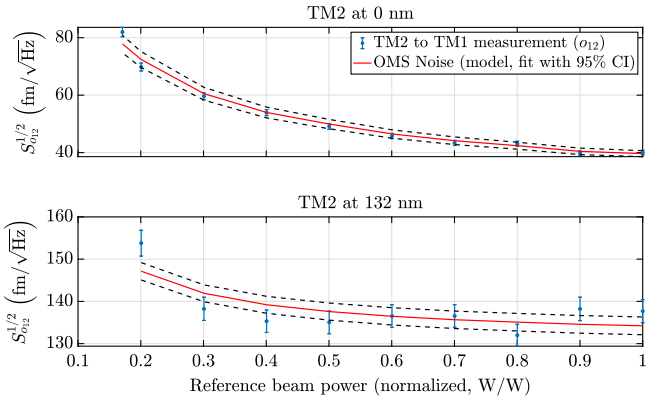

FIG. 16. Noise behavior for varying beam powers (2017-06-17 08:20:00 UTC—2017-06-17 15:00:00 UTC). Top panel: The reference beam power was decreased stepwise, thus lowering the contrast. Bottom panel: Directly after lowering the reference beam power, the second TM was moved to a new (constant) position with maximal 2f-RIN coupling, and the power was increased again with the same steps in reverse. We applied a fit to the total data (all set points combined) with both RIN and ADC noise contributions as free parameters. The coefficients yield RIN $r = (1.08 \pm 0.01) \times 10^{-6}/\sqrt{\text{Hz}}$ and ADC $S_{I_{\text{ADC}}}^{1/2} = (110.4 \pm 2.6)$ pA$/\sqrt{\text{Hz}}$ and are within our previously assumed limits [1]. In the first panel, ADC noise is dominant, while at the 132 nm offset in the second panel RIN is the major contributor. Note: One segment at the lowest power level showed particularly high and unexplained noise and was excluded from the bottom panel.

offset. In this condition, RIN becomes important at high contrasts because of the phase offset and geometric piston.

The RIN value is estimated from a fit to the data and varies between this and other experiments. We also get different results depending of the type of experiment, which is still under investigation. The variations are small enough such that our estimates given here are sufficient to explain the good performance within requirements.

We also fit the equivalent noise current introduced by the ADC, which is likely to vary slightly compared to the ground estimate from years ago. The fit result confirms this by deviating only by about 5%.

The noise model (given in [1] and used in the fit) explains the observed behavior for contrasts between (30 to 98)% in the X12 interferometer. The contrast in the reference interferometer remains unchanged.

4. Noise behavior for varying beam powers

We also investigated the effect of unequal powers between the measurement and reference beam. Instead of changing the wave front overlap due to TM tilts, this also lowers the strength of the heterodyne signal and thus the contrast.

The experiment consisted of stepwise reduction on the reference beam power via the power stabilization loop set-points. After reaching the lowest power, TM2 was shifted via electrostatic actuation to an 132 nm offset, increasing correlated noise sources.

Compared to Sec. III D 3, this experiment also changes the noise couplings in the fixed interferometers regarding power and contrast dependent noise sources.

Figure 16 shows the results for the noise measurements and the model at the two TM positions. As expected, the noise increases towards lower powers due to the $1/C$ dependence. Similarly, at the offset, RIN maximizes its effect and thus decreases the sensitivity to above 150 fm$/\sqrt{\text{Hz}}$.

As in Fig. 15 we fit both the ADC noise and the RIN level using the same model from [1]. While the ADC yields compatible results, the RIN estimate is almost 60% lower, yet still within sensible ranges compared to ground measurements.

One outlier at the lowest power has been removed, which showed a highly increased noise compared to the rest of the data. We suspect nonlinearities in the power stabilization and thermal effects for causing that.

In conclusion, our model explains the observed noise behavior for two of the main parameters of the optical system—the contrast and the power ratio of the two beams for a wide parameter range.

5. Noise budget with grabbed TMs and very low contrast

In April 2017 both TMs were mechanically grabbed. The two longitudinal measurements o_1 and o_{12} and their

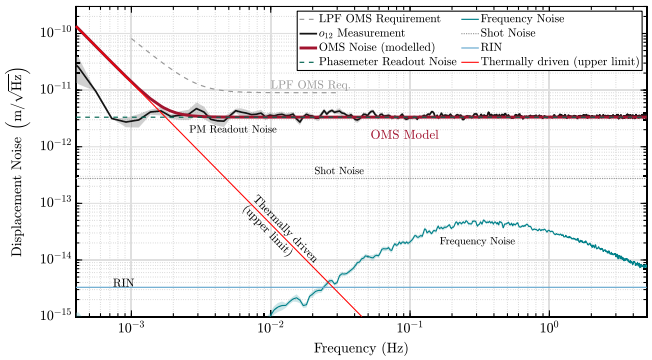

FIG. 17. Noise model applied to an o_{12} measurement with grabbed TMs starting from 2017-04-08 19:55:00 UTC and lasting for 2 hours. Note that the SVN is not visible, since it is around 1×10^{-16} m/$\sqrt{\mathrm{Hz}}$. For the RIN and laser frequency noise contribution, only an upper limit could be estimated.

corresponding noise models are shown in Figs. 17 and 18. DWS is presented in Fig. 19.

The grabbed case corresponds to a very low contrast of 0.6% in X12 and 2% in X1, while the contrast in the reference interferometer remains unchanged. During this measurement period, an upper limit for the RIN level of $r \approx 3 \times 10^{-6}/\sqrt{\mathrm{Hz}}$ was estimated.

The contribution of laser frequency noise is also shown as an upper limit. This limit stems from an experiment to characterize the laser frequency control loop which was executed rather shortly before this noise measurement. While the details of this experiment are under investigation, it can still be used to provide an upper limit for both the o_1 and o_{12} measurements.

In this condition the model reproduces the measured PSD down to mHz frequencies, even with very low contrast, for the longitudinal measurements. As expected

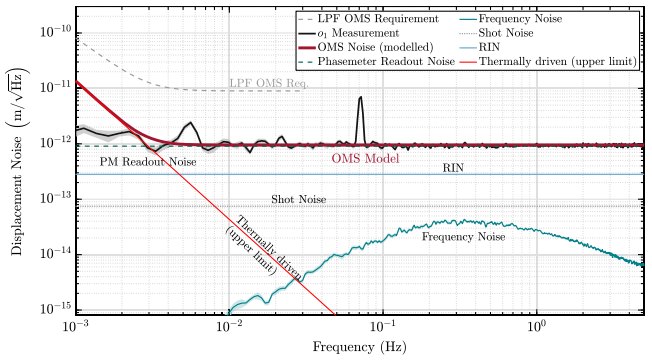

FIG. 18. Noise model applied to an o_1 measurement with grabbed TMs. This data is recorded at the same time as the data shown in Fig. 17. Due to X1 interferometer data measuring a different TM offset and contrast, the shot noise, RIN and frequency noise contributions differ to those of Fig. 17. However, the RIN and laser frequency noise contribution is only provided as an upper limit. Note that the SVN is not visible, since it is well below 1×10^{-15} m/$\sqrt{\mathrm{Hz}}$.

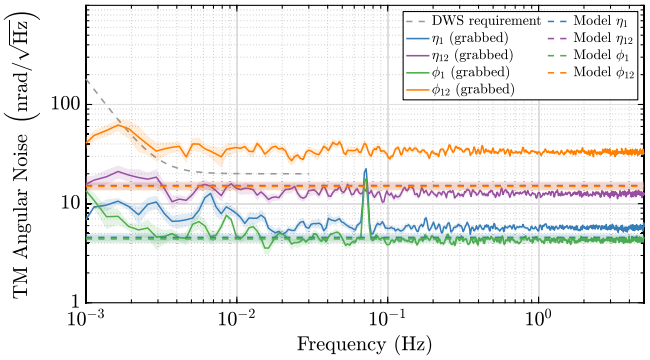

FIG. 19. Noise model applied to DWS with grabbed TMs. This data is recorded at the same time as the data shown in Fig. 17. We observe that the noise level is pseudoflat in all cases down to low frequencies, but has higher magnitude for the differential angles due to the much lower contrast. While the noise model works reasonably well for the X1 interferometer angles, this is not the case for the X12 interferometer angles. Especially the ϕ_{12} channel is deviating by about a factor of 2 from the model. We do not know the reason for this behavior. However, we note that the model still seems to work relatively well with such low contrast that should result in questionable signal quality.

while being grabbed, no TTL coupling or Brownian force noise is visible. As previously, the PM noise is dominating.

The thermally driven noise, as visible at low frequencies in Figs. 17 and 18, suggests that the upper limit stated in [1] and applied here is too conservative below 3 mHz. This implies that the temperature effects of the window transmission, the expansion of the Zerodur baseplate, or the thermal impact of the beam splitters are less significant. Another probable explanation is the presence of common-mode rejection for the balanced beam paths. We previously excluded common-mode effects to obtain an upper limit for these thermally driven effects.

Also note that the data during the grabbed TMs case was recorded during a low temperature period (SC cooling) of about 11.5 °C on the OB.

These cases support our understanding of the sensing noise model, being nominally only visible at high frequencies, extending down to the mHz range.

The peak in o_1 around 70 mHz was already observed and discussed in Fig. 5 and Sec. III A.

In principle, due to grabbing, one would expect the platform jitter (and thus the peak) to be common mode and thus suppressed. Comparing with Fig. 6 we find that the peak is indeed reduced. However, we observe a drift of a few nm between TM1 and the SC, showing that the mechanical grabbing is not perfectly stable. Therefore, some residual coupling seems plausible. The same may hold true for o_{12}, where the differential mode further minimizes the coupling so that it becomes invisible.

These measurements indicate that the sensing noise floor can be well explained in all observable circumstances for both low and high contrasts and the full measurement band.

We observed variations from roughly 32 $\mathrm{fm}/\sqrt{\mathrm{Hz}}$ above 1 Hz for high contrast to 3 $\mathrm{pm}/\sqrt{\mathrm{Hz}}$ at 1 mHz for very low contrast (details see above).

For DWS, see Fig. 19, the model underestimates the noise in ϕ_{12} significantly, while still somewhat matching most of the other channels. The reason for this is unknown.

We conclude that the noise model reflects the observed behavior at frequencies where the sensing noise is expected to be limiting for most of the nominal flight operations.

6. Noise behavior below 1 mHz

In the nominal conditions, white Brownian force noise is dominating at mHz frequencies, with other sources of TM acceleration noise becoming dominant at even lower frequencies [13]. Even with grabbed TMs, at frequencies < 1 mHz, thermomechanical induced motions of the structure holding the TMs is likely dominating the measurement, see also [16].

We have no indication of additional interferometer noise sources, nor of any deterioration of the performance at frequencies below 1 mHz, but we cannot completely exclude them. Based on Fig. 17 we report that even with grabbed TM we reach a sensitivity of approximately 3 $\mathrm{pm}/\sqrt{\mathrm{Hz}}$ at frequencies just below 1 mHz, which would already enable the local TM interferometry on LISA.

E. Limitations of the sensing noise model

Even though the model explains the observed behavior to a good degree, limitations arise mainly due to the fact that LPF, having only a limited telemetry budget, cannot provide all measurements at all times and not at the rate and resolution needed to further improve the model, as well as the fact that we measure a strong real signal at low frequencies (by design).

The physical noises are all well-known contributions that depend on parameters such as contrasts and beam powers, some of which are only known after additional processing took place. For example, individual QPD data was not transmitted to ground, but just averaged channels over interferometer output ports and their quadrants. A more exact model using individual quadrant contributions is therefore unavailable.

In the high frequency range, we are likely affected by aliasing. The processing used aboard LPF employs moving average filters before decimation, which have a limited antialias capability. Thus, we do not always measure the flat spectrum that we understand well and the amount of aliasing cannot be assessed. In addition, we can only extrapolate the noise spectrum for frequencies below about 200 mHz and have to rely on measurements taken with grabbed TMs to indicate the correctness of the model during these relatively high noise states.

Furthermore, measurements of the frequency and reference interferometer at 10 Hz are not available for most of the noise runs, thus rendering estimation of frequency noise and SVN difficult, especially since we cannot differentiate the latter from RIN for most of the mission. At the same time, the actuator noise of the OPD is not measured independently at high frequencies, which is known to affect the spectra.

We also neglect losses arising from realistic beam combiners that are not exactly 50/50 such that the balanced detection will not be ideal.

The estimation of RIN at kHz frequencies is difficult and its level has been estimated to vary throughout the mission. This is likely due to changes in the environmental conditions and can only be observed indirectly. We have only a few more specific indirect RIN measurements that are subject to ongoing analysis.

In addition, we have a large (and difficult to estimate) uncertainty on the ADC noise contribution, which is the dominating noise term in many conditions.

F. Long-term noise behavior over the mission

This part addresses the measurements over the course of the mission for periods where the SC was operated in nominal science mode and only noise was measured.

An overview for the longitudinal and angular readouts is given in Fig. 20 together with a noise model fit and as a histogram in Fig. 22.

1. Data selection and analysis

We selected times during the mission where the SC was kept in nominal operating mode without (known) interfering actions. This excludes commissioning activities, experiments and spacecraft maintenance, DRS (NASA) operations and the spacecraft cooling towards the end of the mission. In a second filtering step, we split the data into 12 min long stretches and discarded segments that include glitches or transients and do not allow a stationary noise power spectrum estimation. The algorithm to filter these transients has a threshold on the amplitude change, i.e., the first derivative in time domain. We used the median absolute deviation (MAD) estimator to specify an equivalent 5σ threshold. From the initial 12916 segments, 140 have been discarded in o_{12} (1.1%), 283 in η_1 (2.2%), 112 in η_{12}, (0.9%), 381 in ϕ_1 (2.9%), and 331 in ϕ_{12} (2.6%).

The selected and filtered times are listed in Table III. For more information on nonstationarities and glitches during the mission see [18,69,70].

We report that even in the presence of short-time nonstationarities the sensitivity was below 2 $\mathrm{pm}/\sqrt{\mathrm{Hz}}$ at high frequencies in the worst case (not shown here, including even more noise only measurements in different configurations).

Every data point in the long-term plots corresponds to those 12 min of data sampled with 10 Hz and averaged over the pseudoflat frequency band between (1.2 to 2.8) Hz.

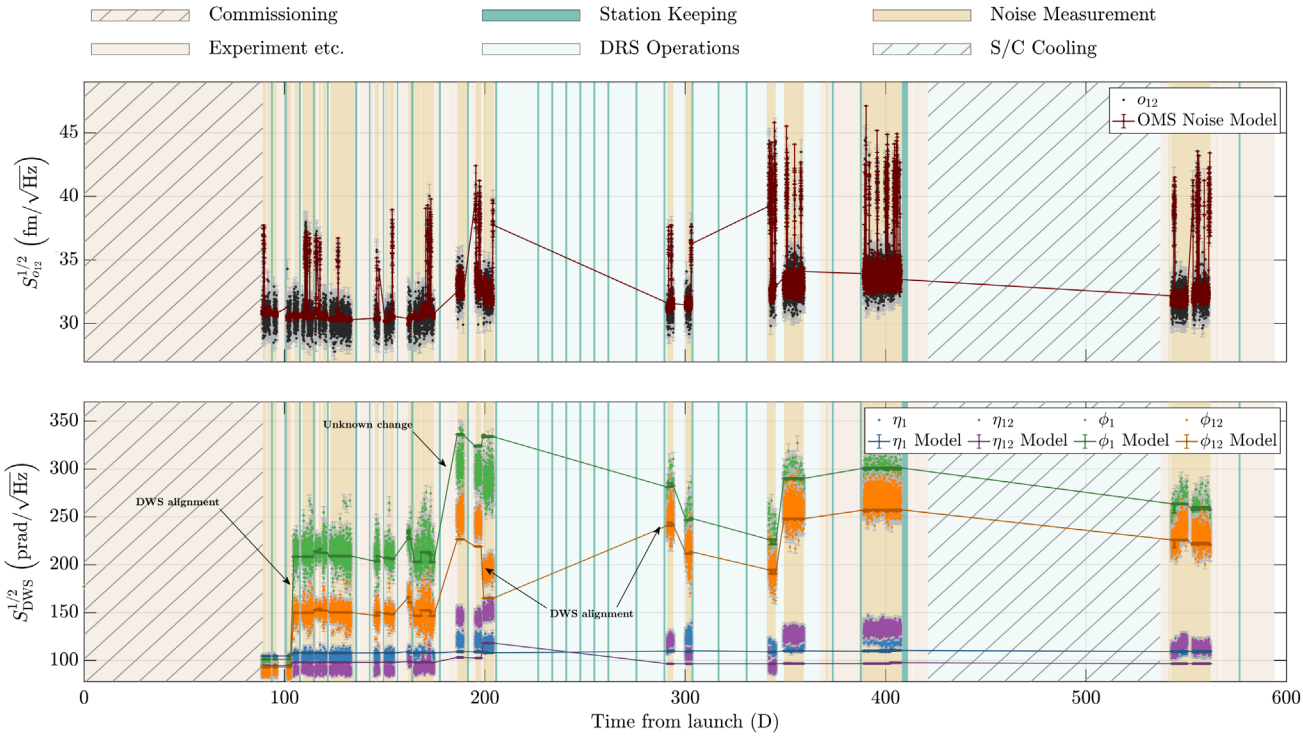

FIG. 20. OMS sensor noise over the mission duration. Shown, in the upper panel, is the longitudinal readout o_{12}, and, in the lower panel, the DWS channels, measuring the angular TM orientations (blue: η_1; purple: η_{12}; green: ϕ_1; orange: ϕ_{12}). Every point corresponds to 12 min of data sampled at 10 Hz, averaged over the pseudoflat and sensor-limited frequency band (1.2 to 2.8) Hz. Also shown are the noise model estimates with solid lines, which have been fitted using the model described in Sec. III B with two fit parameters per segment describing the amount of frequency noise coupling (based on 1 Hz frequency measurements) and the RIN level (which includes SVN due to high correlation), for both of which we do not have independent measurements available. The model is shown with solid lines to increase visibility, but it was only evaluated for the given noise data.

This band has been chosen because we expect the measurement to be sensor noise limited here.

For each of the 12 minute segments the ASD is calculated using 50% overlapping BH92 windows with 36 averages. Every fourth bin is kept to avoid correlations between neighboring bins [71]. At 2 Hz the center bin and two surrounding bins are masked to remove the influence of on-board 1 Hz harmonics as described above.

However, this noise floor may be overestimated due to an imperfect antialiasing caused by the moving average filters used in-flight. Therefore we treat this estimation as an upper bound of the real sensor noise, as there was no access to continuous data with a higher sampling rate.

2. Long-term noise fit

Shown in Fig. 20 are the noise predictions by our models. They use the data from Fig. 21 and fit the RIN value and the frequency noise contribution, the latter based on an estimate of the 1 Hz data. Since we cannot differentiate RIN from SVN here, the estimate can be seen as the effective contribution from both of these.

The fit allows the RIN parameter to vary per noise run, and each noise run is divided into another set of segments, if there is a correlation between the 1 Hz frequency noise estimates and the noise level in o_{12}, to account for the two frequency noise states. Afterwards, all five data channels are jointly fitted per time segment.

While the RIN and SVN contribution are mainly determined from the DWS measurements, the frequency noise contribution estimates relies on the o_{12} data.

Figure 21 shows the main noise model contributions for which we do have independent measurements, showing in what ranges the parameters were stable.

3. Discussion of long-term results

For o_{12}, there are more than two noise regimes apparent. However, one broad level is visible around the median and one upper level around 40 fm/$\sqrt{\text{Hz}}$. The upper noise level represents 9% of the shown data. The lower-noise state has a mean of 31.9 fm/$\sqrt{\text{Hz}}$.

The upper noise levels correlate in time with increased laser frequency noise due to the nonstationary (two-state) behavior of the laser. For the first three measurement timespans, the laser frequency telemetry was available at a sampling frequency of 10 Hz and we found that with the subtraction of the laser frequency noise, the periods of

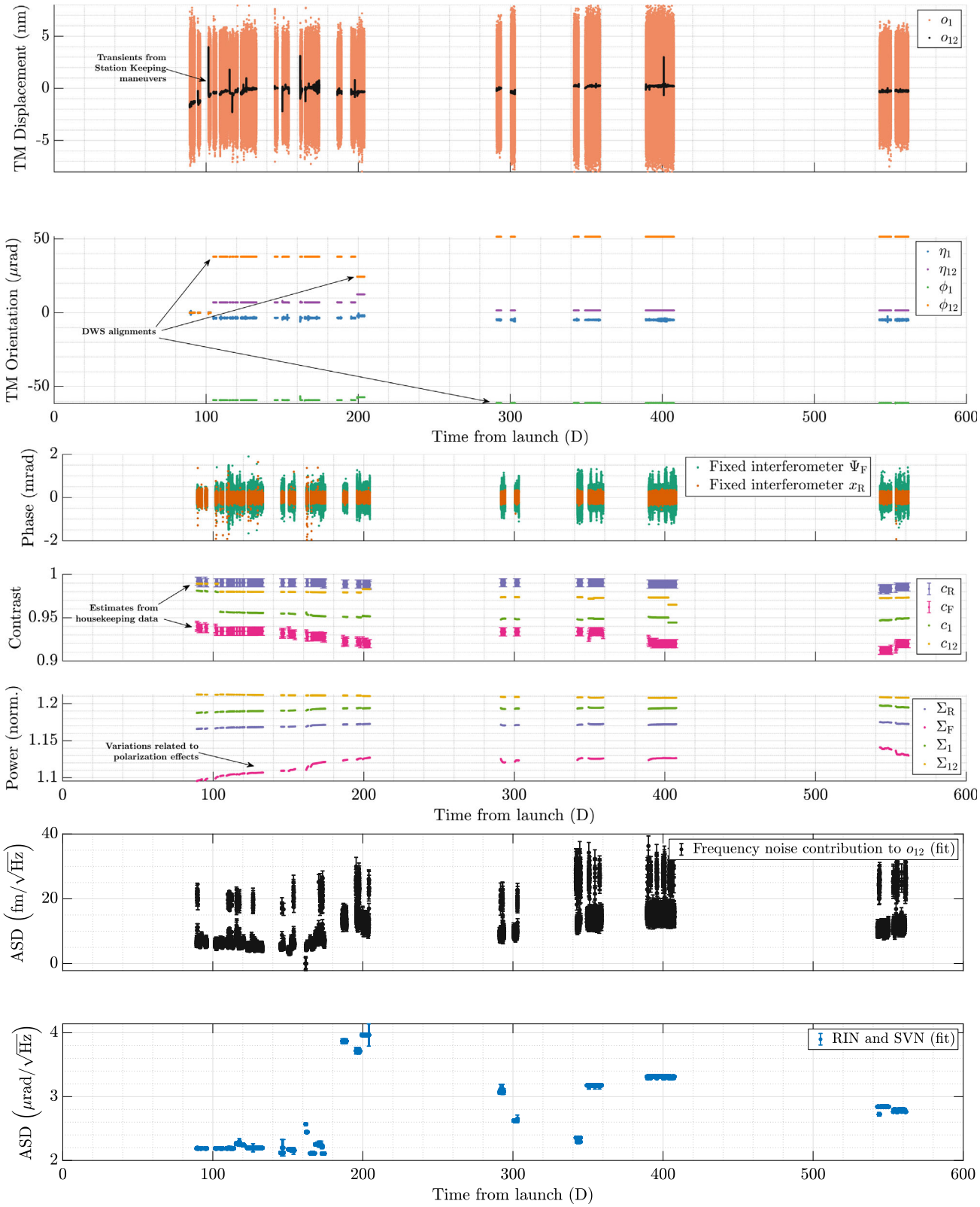

FIG. 21. Main OMS sensor contributions to the noise model over the mission noise runs. In the top five panels we show the time series data for the relevant model contributors. For this plot the measured data channels are sampled with 1 Hz, except for the XF and XR contrast, which is estimated from ADC housekeeping data (reason for higher contrast in c_R than stated in [1]). The bottom two panels show the joint fit results for the two uncorrelated fit parameters from Fig. 20. Note that in segment 2016-11-16 11:05:23 UTC—2016-11-26 07:59:25 UTC the two parameters Σ_R, Σ_F were not available and during 2016-12-26 08:14:59 UTC—2017-01-13 19:57:57 UTC, Σ_R, Σ_{12} had some missing samples. In both cases we interpolated those for the noise model fit.

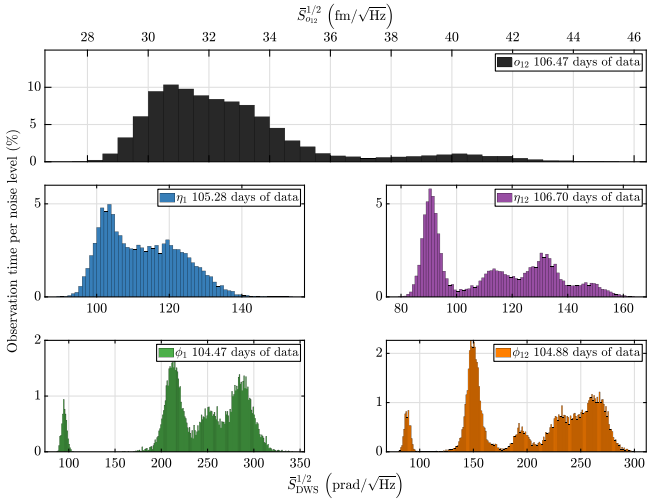

FIG. 22. Histogram of the noise behavior over the mission shown in Fig. 20. The top plot shows the longitudinal differential readout and the lower ones are for DWS. Multimodal distributions are visible, that can be partly explained due to offset dependent noises in DWS, while in o_{12} the upper level is due to states of higher-frequency noise. A detailed discussion is given in the text.

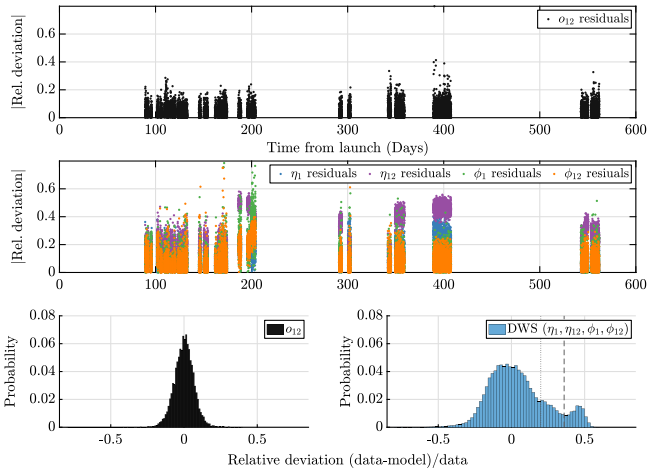

FIG. 23. Relative residuals of the noise fit in Fig. 20. The DWS histogram plot combines the four data channels (blue: η_1; purple: η_{12}; green: ϕ_1; orange: ϕ_{12}). We can see that the biggest (and unexplained) deviation is originating from the η plane and that a large portion is well modeled, given the intrinsic scatter per noise run of a few femtometer in o_{12} and tens of picoradian in DWS.

increased noise can be removed. At later times, the laser frequency telemetry was only available at 1 Hz which does not allow for this subtraction.

Figure 22 shows the histogram of the noise spectrum estimation. The y-axis shows the percentage of time spent at a specific noise level with respect to the total measurement length per observable. The bin width is 0.5 fm/$\sqrt{\text{Hz}}$ for o_{12} and 1 prad/$\sqrt{\text{Hz}}$ for DWS.

Based on the segment analysis defined above we find that the measurement in o_{12} varies between 27.8 fm/$\sqrt{\text{Hz}}$ and 44.1 fm/$\sqrt{\text{Hz}}$ with a median of $32.0^{+2.4}_{-1.7}$ fm/$\sqrt{\text{Hz}}$. The values are based on the 16th, 50th, and 84th percentiles of the histogram.

The DWS signals show a much broader distribution of varying modes with maxima between (86 to 290) prad/$\sqrt{\text{Hz}}$. We attribute this behavior (as far as we can explain) to offset dependent noise couplings (such as RIN, SVN). During specific times of the mission, the TM orientation was changed, causing varying noise levels. See Secs. III B and III D for details.

In DWS, the frequency noise is highly correlated and well phase-matched on all photodiode quadrants and therefore subtracts to a large degree when forming the DWS signals (by differencing the left/right, up/down quadrant phases). As expected, we see no effect from changing frequency noise levels.

The noise levels of Fig. 20 show that the OMS measurements have been much more sensitive than expected, enabling a level of investigation unpredicted at the beginning of the mission.

The models confirm that we have a good understanding of the noise (similar to what was shown in [1]), even though we cannot explain all of the changes in the noise over the mission in DWS.

The remaining discrepancy (residuals are shown in Fig. 23) between the model and the fit have been investigated to a great detail but a definite explanation could not be identified. We deem an influence of the OB temperature rather unlikely, since it is very stable and has no correlated changes, as can be seen by comparing with the temperature data given in [66].

The same holds true for a change in phasemeter readout noise which is furthermore constrained by the o_{12} behavior observed during the course of the mission. A data processing error also seems not very likely since the same quadrant data is used for all the measurements and a processing error should lead to similar noise changes in all channels which we do not observe.

Moreover, based on the observed, asymmetric change in the system noise levels in DWS (before 06.06.2016, day 186 from launch), we were searching for an explanation which is strongly suppressed in the longitudinal readout. However, the available data does not allow us to reject a hypothesis related to changing laser behavior or ghost beams.

For most laser housekeeping data, we are limited by the sampling frequency of only 0.2 Hz. Laser intensity and frequency fluctuations can only be included as estimates since no direct measurement in the required frequency ranges are available.

The optical fibres should always deliver the same mode by design. The polarization of the light on the OB is known to change over the course of the mission (see [72]) and a

weak correlation with changing RF amplitudes used to drive the AOMs may be present.

Even though we could observe a few periods during which the pump current and the laser temperature appear correlated to the noise in some of the observed channels, the exact mechanism from a laser setting to a change of the noise above 1 Hz is not clear, appears nonlinear and no definite, repeating pattern could be found.

Furthermore, in between two noise runs, we found a period where the laser heater set point was correlated to the noise level. However, at other times in between noise runs, we cannot confirm this observation and thus we conclude that this is not the main driver of the observed changes in noise level.

In addition, it should be noted that the DWS spectra were not always perfectly flat. This could possibly point to aliasing which is not modeled well enough or a higher influence of the OPD actuator with the observed spikes (Sec. III B 2). But again, we are limited by the data rate of the telemetry. There are just a few dedicated experiments where 100 Hz data was available, which are very short and always only cover a small portion of the channels.

Since the reason for the observed changes in the DWS noise levels over the mission duration could not be found yet, we can also not estimate whether this behavior is related to any specifics of LPF and the OMS or if it is a more general aspect limiting the common-mode noise rejection in DWS compared to the much less affected longitudinal measurement.

Nonetheless, the agreement between the model and the data is good in most cases and much below any required level.

IV. LONG-TERM STABILITY OF THE OMS

The long-term stability of the OMS is of relevance with regard to the three to six times longer LISA mission. Besides typical lifetime limiting effects like dust and operational abrasion, the cosmic radiation is additionally penetrating the components.

The long-term performance of the photodiodes (PDs) is of special interest, since they are relevant for the shot noise contribution in LISA and, as electro-optical components, especially sensitive to cosmic particle radiation. Furthermore, the mechanical stability of the OB is important, since the interferometry alignment relies on it.

In the following, stability analyses of different subsystems of the OMS are described.

A. OB stability

The mechanical stability of the OB was actively monitored during flight, using dedicated, so-called spot position measurements.

For this, the beams were turned off one after another to measure the beam spot positions on all OB QPDs and identify possible distortions of the OB baseplate or changes in the alignment.

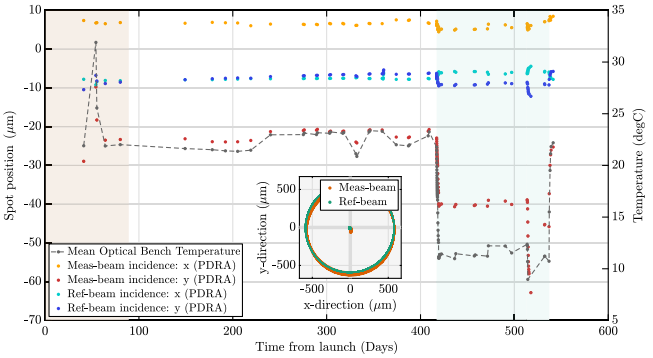

FIG. 24. Spot position changes over the course of the mission and the mean optical bench temperature. Highlighted are the commissioning phase and the SC cooling. The inset figure shows the corresponding (simulated) beam walks and beam diameters of the two beams on the PDRA diode with its 45 μm slits between quadrants. The total diameter of the diodes active surface is 5 mm. The temperature measurements between day 513 and 537 from launch (at the lowest temperatures) were limited by the temperature sensors. The real temperature was lower during this time span. The measurements from other sensors suggest a decrease of down to almost 0 °C.

The procedure was executed multiple times covering more than 1.5 years of the mission (see Fig. 24).

During all of these measurements, the spot positions of both beams changed less than 5 μm in horizontal "x" direction and for the reference beam less than 7 μm in vertical "y" direction.

Only the measurement beam's spot positions showed a larger deviation in vertical direction. This is especially interesting in combination with a frequent monitoring during the so-called cool-down phase. Here, temperature changes of more than 20 °C occurred without an impact on the beam spot positions above 43 μm. In consequence, the OB was found to be highly stable against temperature changes.

A detailed examination of the spot position changes due to the cool down of the SC shown in Fig. 24 reveals that the beams' spot positions are more stable in the horizontal direction, i.e., parallel to the optical bench surface.

When the SC was cooled down, the spot positions decreased in along the vertical axis, i.e., the beams' incident point came closer to the OB surface. This effect was stronger for the measurement than for the reference beam. This beam walk most likely results from a down-tilt of the beams at their fiber injector optical subassemblies (FIOSs). From ground tests of these, we know that the beams tilt less than 3 μrad per °C temperature difference. Since the measurement beams propagate a longer path between its FIOS and diode PDRA, the resulting spot position change is expected to be larger.

Additionally, the particular spot position readouts suggest a bending of the entire OB yielding additional beam tilts and beam walk on the photodiodes. In pre-launch tests it was demonstrated that the center of the OB can lift or sink up to 1.7 μm with respect to its outer edges due to mechanical stresses of its mounts.

Such a behavior is likely a consequence of the thermally induced stress regarding the mechanical structures holding the OB, as also discussed in [69].

In summary, both, the beam tilt at the FIOS and the OB deformation are small even for the strong temperature changes intentionally applied during the cooling period of LPF.

B. PD responsivity

The responsivity of the LPF interferometer diodes was monitored with a dedicated experiment using the radiation pressure to the TMs as a power reference signal. The experiment was executed three times during the mission resulting in a monitoring duration of 1.5 years. During this monitoring period no degradation could be observed within errors of 1%.

A comparison to preflight measurements, in contrast, showed a small degradation of the responsivity of 4% for the whole flight phase. A systematic error of up to 3% had to be taken into account in-flight. It is assumed to originate from two minor solar energetic particless (SEPs) events between launch and the PD monitoring period that emitted solar protons at relevant energies.

However, there was no direct observation of an SEP event during the monitoring duration. In consequence, the "background" cosmic radiation in the declining solar cycle was found to be of low relevance for the PD responsivity.

Nonetheless, a significant impact of SEP events with low particle energies can be supposed, although no direct observation during the monitoring duration was possible. By that, the results further agree with preflight radiation tests with flight spare PDs.

We also refer to [72–74].

C. TM reflectivity and optical window transmittance

In addition to the radiation pressure measurement, the TM reflectivity in combination with the optical window transmittance was monitored. This joint parameter could be extracted from the beam spot position measurements. It was found that the TM reflectivity and optical window transmittance changes less than 0.2% during the whole monitoring duration of 392 days [72].

Thus, no degradation of the TM surface or the optical window (OW) transmittance could be observed from cosmic radiation or dust, within the measurement accuracy.

D. Beam polarization

The spot position measurements showed unexpected significant fluctuations in the single beam powers, despite the active beam power control loop. This is for example visible in Σ_F in Fig. 21. During certain periods of the mission, this noise was correlated to temperature measurements.

The observation was best explained by changes of the polarization of the light (see the in-depth modeling in [72]). To be more precise, in the measurement beam, the ratio of the undesired P-polarization, compared to the S-polarization aimed for, amounts to 1.7% and in the reference beam to 4.5%. It is assumed that the off-nominal polarized light originates in the fibers that deliver the light to the OB. However, the fiber couplers mounted on the OB were designed to clean the polarization (as explained in Sec. II B).

The detailed investigation found a decrease in the polarization extinction ratio of the polarizing beam splitter inside the fibre couplers in vacuum due to the out-gassing of water to be the best explanation for the polarization fluctuations. However, this explanation is not sufficient for all of the P-polarized light on the OB.

The P-polarized light may impact the OMS measurements via two mechanisms. The first of these is the decrease of the balancing detection efficiency which can then impact the suppression of RIN at the heterodyne frequency.

However, with the observed RIN noise levels during the mission, this effect is negligible.

The second mechanism concerns additional phase noise resulting from the interference of the two P-polarized beams in each interferometer. This can yield a readout noise depending on the relative phase of the S- and P-polarized light but the LPF measurements restrict this effect to be below mHz frequencies.

E. Laser and phasemeter performance

The laser and the phasemeter worked reliably throughout the mission.

We chose a measured contrast in the reference interferometer above 85% as a parameter to indicate that these two units are operating well. This choice was made because the reference interferometer measurement is unaffected during a large number of manoeuvres and this level of contrast can only be reached if both beams are operational and well centered on the PDs. In addition, the ADC utilization parameters are a result of the phasemeter and thus the availability of reasonable data indicates it was operating.

We defined the mission duration to begin with the beginning of nominal operations on March 1st, 2016 at 08:00 UTC and to end on July 1st, 2017 at 08:00 UTC.

We find that the laser and phasemeter unit reached a duty cycle of 99.4% with regard to the total mission duration. If we consider only the times of the contrast in the reference

interferometer above 85% with respect to the total mission duration, we find a duty cycle of 99.0%. The latter also includes experiments that deliberately lowered the contrast.

In general the laser power stability (RIN) was within requirements and not the limiting noise source, as far as we were able to estimate from indirect measurements.

F. Contamination

The optical transmission from the laser to the PDs was estimated by looking at the pump current, the RF amplifier powers and the measured optical power on the QPDs during the radiation pressure measurements [72].

However, since the polarization state coming out of the optical fibers is known to fluctuate, the main source of power losses is expected to originate from reflections at the polarizing beam splitters. Since the reflected power is not monitored, the accuracy of an estimate for the optical transmission is limited.

Nevertheless, no common increase of the pump current and RF amplifier power could be observed within the three radiation pressure measurements, although the OB power stayed comparably constant. A contamination of the optical component surfaces on the OB would further lead to a common decrease of the power on the interferometer diodes, since the power control pick off is located directly after the fiber out-couplers.

The specific OB model that was used to fit the level of parasitic polarization, however, showed no common decrease of the power at the QPDs.

In consequence, no significant long-term contamination of the optical components during flight could be observed.

V. OPERATIONAL CHALLENGES

The impressive performance reported here maintained throughout the mission. Nevertheless, some issues were observed during flight and had to be dealt with operationally, leading to "lessons-learned" for future similar sensor implementations.

An example of such an issue arose due to the fact that the laser system was more sensitive to the environmental temperature than expected, and so consideration of the platform environment for such units should be more carefully accounted for in future designs.

In this case, implementation of a dedicated temperature control system, for example, would have reduced the reliance on complex operational procedures. In addition, as predicted from on-ground tests, the slow power control loop as implemented was too strongly coupled to the temperature of the laser, and as such was not employed during operations.

The analysis of the in-flight data has allowed us to characterize the OMS to a significant level, however, the lack of simultaneous access to all of the raw phasemeter data (which was not possible given the telemetry restrictions of the mission) and the missing on-board clock synchronization made certain (noncritical) diagnostic and scientific investigations difficult and sometimes impossible.

An out-of-loop monitor of the single optical beams was not part of the design, which limits what we can say about the force noise produced by power fluctuations in the beam. In the flight system we have to infer this from isolated off-line measurements of the single beams made by turning one beam off.

The ability to align the TMs prior to release to allow full validation of the OMS readout in the measurement band would have been desirable. In the event, we can only surmise that the system performance at low frequencies was consistent with that which we observed at high frequencies.

VI. CONCLUSIONS

The LPF OMS was designed to meet a differential displacement noise level of $9\,\mathrm{pm}/\sqrt{\mathrm{Hz}}\times\sqrt{1+(3\,\mathrm{mHz}/f)^4}$ over a frequency range of (1 to 30) mHz, and in ground testing it met this goal.

The in-flight performance was significantly better than this goal, with a residual median noise level of $32.0^{+2.4}_{-1.7}$ $\mathrm{fm}/\sqrt{\mathrm{Hz}}$ at frequencies where TM motion was not limiting. Above 0.4 Hz the noise was typically smaller by more than a factor 100 compared to on-ground tests. A similar improvement is true for DWS angular signals.

This excellent performance during science operations of LISA Pathfinder has allowed us to investigate in great detail the noise behavior of the system. We could develop and verify a comprehensive model which is valid over a wide variety of sensor operating conditions. This analysis significantly increases the confidence in the model. When applying the sensing noise model to LPF noise measurements, we explain the averaged noise in the frequency range from (1.2 to 2.8) Hz in the o_{12} measurement to better than 20% for most of the mission. A number of additional investigations (see Table I) has led to deeper understanding of the system, but also to some questions which could not be fully solved, partly due to the operational constraints (see Sec. V). One of these open questions entails the detailed understanding of the OPD, including the discrepancy between measured and expected loop behavior. Another one is the discrepancy between the RIN fit results from TM tilt experiments and those from longitudinal step experiments, which stays well below the requirements. We only found a single angular measurement in the grabbed TMs case for very low contrast, where we could not identify why the model for the ϕ_{12} data was explaining only a fraction of the noise. Regarding the sensitivity over the mission, a few changes in DWS could not be fully explained by our model. As we could not identify the mechanism behind these changes, it is not possible to estimate the relevance of this observation for similar optical

setups. However, all of these measurements are orders of magnitude below the required accuracy level.

The deep understanding generated through the detailed model is very beneficial in the design of the OMS for LISA which has performance characteristics very similar to those demonstrated on LPF.

The long term performance of the OMS showed no major degradations that could harm the LISA mission when extrapolated to longer mission durations. Solely the LPF polarization stability would not be good enough for LISA. However, since the origin of the polarization fluctuations could be identified, the effect can easily be avoided by an appropriate polarization filter.

LPF has shown that high precision optical systems such as the OMS can work even better in the stable environment of a specialized space platform than demonstrated on ground. Moreover, the OMS has proven to be highly stable and reliable in itself, which is a cornerstone for the much longer LISA mission.

ACKNOWLEDGMENTS

This work has been made possible by the LISA Pathfinder mission, which is part of the space-science programme of the European Space Agency. The Albert Einstein Institute acknowledges the support of the German Space Agency, DLR. The work is supported by the Federal Ministry for Economic Affairs and Energy based on a resolution of the German Bundestag (FKZ 50OQ0501, FKZ 50OQ1601, and FKZ 50OQ1801). We also acknowledge the support by the Deutsche Forschungsgemeinschaft (DFG, German Research Foundation) under Germany's Excellence Strategy—EXC-2123 QuantumFrontiers—390837967. The French contribution has been supported by the CNES (Accord Specific de projet CNES 1316634/CNRS 103747), the CNRS, the Observatoire de Paris and the University Paris-Diderot. E. P. and H. I. would also like to acknowledge the financial support of the UnivEarthS Labex program at Sorbonne Paris Cité (ANR-10-LABX-0023 and ANR-11-IDEX-0005-02). The Italian contribution has been supported by ASI (Grant No. 2017-29-H.1-2020 "Attività per la fase A della missione LISA") and Istituto Nazionale di Fisica Nucleare. The Spanish contribution has been supported by Contracts No. AYA2010-15709 (MICINN), No. ESP2013-47637-P, No. ESP2015-67234-P, and No. ESP2017-90084-P (MINECO). Support from AGAUR (Generalitat de Catalunya) Contract No. 2017-SGR-1469 is also acknowledged. M. N. acknowledges support from Fundacion General CSIC (Programa ComFuturo). F. R. acknowledges an FPI contract from MINECO. The Swiss contribution acknowledges the support of the ETH Research Grant No. ETH-05 16-2 and the Swiss Space Office (SSO) via the PRODEX Programme of ESA. L. F. is supported by the Swiss National Science Foundation. The UK groups wish to acknowledge support from the United Kingdom Space Agency (UKSA), the Scottish Universities Physics Alliance (SUPA), the University of Glasgow, the University of Birmingham, and Imperial College London. J. I. T. and J. S. acknowledge the support of the US National Aeronautics and Space Administration (NASA). N. K. would like to thank for the support from the CNES Fellowship. The LISA Pathfinder Collaboration would like to acknowledge Professor P. B. (deceased 30 March 2017), Professor J. A. L. (deceased 30 September 2012), and L. G. B. (deceased 29 May 2020) for their remarkable contribution to the LISA Pathfinder science.

APPENDIX A: PARAMETER SUMMARY

x_{12}: Displacement measurement between the two TMs.
x_1: Displacement measurement between TM1 and the SC.
x_R: Longitudinal reference interferometer measurement.
x_F: Longitudinal frequency interferometer measurement.
Ψ_F: Longitudinal frequency interferometer measurement with subtraction of x_R processed onboard.
o_{12}: Main telemetry channel of the differential displacement between the two TMs, processed onboard via $x_{12} - x_R$, with a calibration factor to scale to [m].
o_1: x_1 with subtraced reference phase, processed onboard via $x_1 - x_R$, with a calibration factor to scale to [m].
ϕ_1: Calibrated xy-plane DWS TM1 angle, measured in X1.
η_1: Calibrated xz-plane DWS TM1 angle, measured in X1.
ϕ_{12}: Calibrated xy-plane DWS differential TM angle, measured in X12.
η_{12}: Calibrated xz-plane DWS differential TM angle, measured in X12.
ϕ_2: Calibrated xy-plane DWS TM2 angle, processed onboard from linear combinations of X1 and X12.
η_2: Calibrated xz-plane DWS TM2 angle, processed onboard from linear combinations of X1 and X12.

APPENDIX B: OMS EXPERIMENTS AND SELECTED "NOISE RUNS" DURING THE LPF MISSION

In this appendix we give a list of dedicated experiments that were performed during the mission with the aim to characterize the OMS in Tables I and II.

Some few investigations have missing data and are not mentioned. Commissioning activities are also not listed.

Most of the experiments in this list have been used in the analysis for this publication.

Furthermore, the segments used in the long-term analysis are stated in Table III.

TABLE I. List of OMS specific experiments during the LPF mission. More details on most of these can be found in [64,65].

Nr.	Experiment	Start (UTC)	End (UTC)	Description
1	Engineering days	2016-03-14 08:00:00	2016-03-17 20:00:00	Sinusoidal injections to the lateral Degree-of-Freedom (DOF) of both TMs at different set-points and final TM realignments for TTL suppression.
2	Thermal stability experiments	2016-03-16	2017-06-17	Experiments testing various OMS components, see [66], given for completeness.
3	Single quadrant investigations 1	2016-04-23 13:30:00	2016-04-23 13:50:22	Attempt to characterize limited number of single quadrants with short 100 Hz segments.
4	Longitudinal step experiment 1	2016-04-25 08:00:00	2016-04-26 08:00:00	Longitudinally shift TM2 to different set points to analyze noise behavior and fit RIN.
5	Single quadrant investigations 2	2016-04-25 12:50:02	2016-04-25 13:40:22	Attempt to characterize limited number of single quadrants with short 100 Hz segments.
6	Beam power modulation	2016-05-30 08:00:00	2016-05-31 08:00:00	Modulation of reference beam, during thermal experiments.
7	Beam power modulation	2016-05-31 20:00:00	2016-06-01 16:00:00	Modulation of measurement beam.
8	OPD loop characterization experiment	2016-06-01 16:35:08	2016-06-01 17:05:30	Estimate controller transfer function and open-loop transfer function.
9	Frequency loop characterisation experiment	2016-06-01 17:35:10	2016-06-01 18:06:00	Estimate transfer functions from laser frequency modulation.
10	Frequency loop open	2016-06-02 00:42:00	2016-06-02 05:40:00	Data to compare to ground and closed-loop measurement.
11	DWS angular tilt experiment 1	2016-06-02 08:30:00	2016-06-03 07:25:00	Tilt TM2 to different angular set-points to analyze noise behavior and fit RIN.
12	OPD loop open	2016-06-11 12:02:31	2016-06-12 00:00:59	Data to compare to ground and closed-loop measurement.
13	Single quadrant investigations 3	2016-06-12 15:10:00	2016-06-12 16:30:21	Attempt to characterize limited number of single quadrants with short 100 Hz segments.
14	OPD loop characterization experiment	2016-06-13 04:35:05	2016-06-13 05:32:05	Estimate controller transfer function and open-loop transfer function.
15	Frequency loop characterization experiment	2016-06-13 06:05:10	2016-06-13 06:55:49	Estimate transfer functions from laser frequency modulations.
16	Beam power modulation	2016-06-13 21:27:30	2016-06-14 21:27:30	Modulation of reference beam, during thermal experiments.
17	Path length mismatch experiment	2016-06-14 21:20:00	2016-06-15 06:42:00	Estimate the path length mismatch from laser frequency modulations.
18	Frequency loop open	2016-06-15 02:53:00	2016-06-15 05:29:59	Data to compare to ground and closed-loop measurement.
19	OPD loop open	2016-07-07 10:57:01	2016-07-07 11:20:20	Data to compare to ground and closed-loop measurement.
20	OPD loop open	2016-07-07 11:23:00	2016-07-07 11:44:27	Data to compare to ground and closed-loop measurement.
21	DWS derisk with large tilts	2017-01-17 07:00:00	2017-01-18 07:25:00	Tilt TM1 and TM2 to large angular set points in preparation for DWS tilt 2 experiment, check for too low contrast.

(Table continued)

TABLE I. *(Continued)*

Nr.	Experiment	Start (UTC)	End (UTC)	Description
22	SVN experiment 1	2017-01-18 06:27:05	2017-01-18 06:53:32	Injection of phase ramps via the OPD loop to measure SVN.
23	Short cross-talk experiment	2017-01-21 00:30:00	2017-01-21 05:30:00	Sinusoidal injections to the lateral DOF of both TMs at one set point.
24	Beam power modulation	2017-01-21 08:00:00	2017-01-22 10:30:00	Multiple modulations and counter modulation experiments with varying depths.
25	Frequency loop characterisation experiment	2017-01-22 10:35:10	2017-01-22 11:26:49	Estimate transfer functions from laser frequency modulations.
26	Path length mismatch experiment	2017-01-22 12:05:00	2017-01-22 14:59:00	Estimate the path length mismatch from laser frequency modulations.
27	Frequency loop open	2017-01-22 16:45:00	2017-01-23 02:59:59	Data to compare to ground and closed-loop measurement.
28	SVN experiment 2	2017-02-02 20:35:00	2017-02-04 21:30:00	Injection of phase ramps via the OPD loop to measure SVN, with longitudinal offsets.
29	Longitudinal step experiment 2	2017-02-02 20:36:00	2017-02-04 21:36:00	Longitudinally shift TM2 to different set-points to analyze noise behavior and fit RIN. Includes OPD ramps at offsets for SVN analysis and unbalanced segments.
30	Long cross-talk experiment	2017-02-04 21:00:00	2017-02-06 23:00:00	Series of short cross-talk experiments performed at different set-points of the various DOFs.
31	DWS angular tilt experiment 2	2017-02-06 23:06:00	2017-02-08 22:55:00	Tilt TM1 and TM2 to different angular set-points to analyse noise behavior and fit RIN. Includes unbalanced segments.
32	Frequency loop characterization experiment	2017-04-06 22:30:08	2017-04-06 23:50:42	Estimate transfer functions from laser frequency modulations.
33	Reference beam power modulation	2017-06-17 08:20:00	2017-06-17 15:00:00	Steps to lower the reference beam power, shift TM2 and increase the power again.
34	OPD loop open	2017-06-25 16:43:10	2017-06-25 17:55:10	Data to compare to ground and closed-loop measurement.
35	Direct RIN measurement at $2f$	2017-07-11 00:00:00	2017-07-12 03:32:00	Attempt to measure 2f-RIN directly by shifting the SBDFT to 2 kHz.

TABLE II. Spot position measurements; MB Measurement beam, RB reference beam. In-flight more measurements have been taken for which a few had missing data. Those are not given here.

Nr.	Experiment	Start (UTC)	End (UTC)
1	RB off	2016-04-30 12:00:32	2016-04-30 12:04:09
2	MB off	2016-04-30 12:05:03	2016-04-30 12:08:32
3	RB off	2016-05-29 12:00:32	2016-05-29 12:04:09
4	MB off	2016-05-29 12:05:03	2016-05-29 12:08:32
5	RB off	2016-06-12 00:01:32	2016-06-12 00:05:09
6	MB off	2016-06-12 00:06:03	2016-06-12 00:09:32
7	RB off	2016-06-25 12:05:57	2016-06-25 12:09:41
8	MB off	2016-06-25 12:10:32	2016-06-25 12:14:09
9	RB off	2016-07-09 18:06:37	2016-07-09 18:10:07
10	MB off	2016-07-09 18:11:07	2016-07-09 18:14:37
11	RB off	2016-07-30 18:06:37	2016-07-30 18:10:07
12	MB off	2016-07-30 18:11:07	2016-07-30 18:14:37
13	RB off	2016-08-20 12:03:25	2016-08-20 12:07:19
14	MB off	2016-08-20 12:07:58	2016-08-20 12:11:45
15	RB off	2016-09-03 12:03:26	2016-09-03 12:07:20
16	MB off	2016-09-03 12:07:55	2016-09-03 12:11:50
17	RB off	2016-09-04 12:03:26	2016-09-04 12:07:20
18	MB off	2016-09-04 12:07:55	2016-09-04 12:11:50
19	RB off	2016-09-17 12:03:26	2016-09-17 12:07:20
20	MB off	2016-09-17 12:07:55	2016-09-17 12:11:50
21	RB off	2016-09-18 12:03:26	2016-09-18 12:07:20
22	MB off	2016-09-18 12:07:55	2016-09-18 12:11:50
23	RB off	2016-10-01 12:03:26	2016-10-01 12:07:20
24	MB off	2016-10-01 12:07:55	2016-10-01 12:11:50
25	RB off	2016-10-02 11:03:26	2016-10-02 11:07:20
26	MB off	2016-10-02 11:07:55	2016-10-02 11:11:50
27	RB off	2016-10-15 12:03:26	2016-10-15 12:07:20
28	MB off	2016-10-15 12:07:55	2016-10-15 12:11:50
29	RB off	2016-10-16 11:03:26	2016-10-16 11:07:20
30	MB off	2016-10-16 11:07:55	2016-10-16 11:11:50
31	RB off	2016-10-29 12:03:26	2016-10-29 12:07:20
32	MB off	2016-10-29 12:07:55	2016-10-29 12:11:50
33	RB off	2016-10-30 12:03:26	2016-10-30 12:07:20
34	MB off	2016-10-30 12:07:55	2016-10-30 12:11:50
35	RB off	2016-11-12 12:03:26	2016-11-12 12:07:20
36	MB off	2016-11-12 12:07:55	2016-11-12 12:11:50
37	RB off	2016-11-13 15:33:26	2016-11-13 15:37:20
38	MB off	2016-11-13 15:37:55	2016-11-13 15:41:50
39	RB off	2016-11-26 12:03:26	2016-11-26 12:07:20
40	MB off	2016-11-26 12:07:55	2016-11-26 12:11:50
41	MB off	2016-11-27 12:03:15	2016-11-27 12:07:20
42	MB off	2016-11-27 12:07:26	2016-11-27 12:11:25
43	MB off	2016-11-27 12:11:31	2016-11-27 12:15:30
44	MB off	2016-11-27 12:15:36	2016-11-27 12:19:35
45	RB off	2016-12-11 12:03:26	2016-12-11 12:07:20
46	MB off	2016-12-11 12:07:55	2016-12-11 12:11:50
47	RB off	2016-12-24 12:03:26	2016-12-24 12:07:20
48	MB off	2016-12-24 12:07:55	2016-12-24 12:11:50
49	RB off	2016-12-25 12:03:26	2016-12-25 12:07:20
50	MB off	2016-12-25 12:07:55	2016-12-25 12:11:50
51	RB off	2017-01-14 12:03:26	2017-01-14 12:07:20
52	MB off	2017-01-14 12:07:55	2017-01-14 12:11:50
53	RB off	2017-01-15 12:03:26	2017-01-15 12:07:20
54	MB off	2017-01-15 12:07:55	2017-01-15 12:11:50
55	RB off	2017-01-23 08:18:22	2017-01-23 08:22:18
56	MB off	2017-01-23 08:23:08	2017-01-23 08:26:52
57	RB off	2017-01-23 09:18:22	2017-01-23 09:22:18
58	MB off	2017-01-23 09:23:08	2017-01-23 09:26:52
59	RB off	2017-01-23 10:18:22	2017-01-23 10:22:18
60	MB off	2017-01-23 10:23:08	2017-01-23 10:26:52
61	RB off	2017-01-23 11:18:22	2017-01-23 11:22:18
62	MB off	2017-01-23 11:23:08	2017-01-23 11:26:52
63	RB off	2017-01-23 12:18:22	2017-01-23 12:22:18
64	MB off	2017-01-23 12:23:08	2017-01-23 12:26:52
65	RB off	2017-01-23 13:18:22	2017-01-23 13:22:18
66	MB off	2017-01-23 13:23:08	2017-01-23 13:26:52
67	RB off	2017-01-23 14:18:22	2017-01-23 14:22:18
68	MB off	2017-01-23 14:23:08	2017-01-23 14:26:52
69	RB off	2017-01-23 15:18:22	2017-01-23 15:22:18
70	MB off	2017-01-23 15:23:08	2017-01-23 15:26:52
71	RB off	2017-01-23 16:18:22	2017-01-23 16:22:18
72	MB off	2017-01-23 16:23:08	2017-01-23 16:26:52
73	RB off	2017-01-23 17:18:22	2017-01-23 17:22:18
74	MB off	2017-01-23 17:23:08	2017-01-23 17:26:52
75	RB off	2017-01-23 18:18:22	2017-01-23 18:22:18
76	MB off	2017-01-23 18:23:08	2017-01-23 18:26:52
77	RB off	2017-01-23 19:18:22	2017-01-23 19:22:18
78	MB off	2017-01-23 19:23:08	2017-01-23 19:26:52
79	RB off	2017-01-23 20:18:22	2017-01-23 20:22:18
80	MB off	2017-01-23 20:23:08	2017-01-23 20:26:52
81	RB off	2017-01-23 21:18:22	2017-01-23 21:22:18
82	MB off	2017-01-23 21:23:08	2017-01-23 21:26:52
83	RB off	2017-01-23 22:18:22	2017-01-23 22:22:18
84	MB off	2017-01-23 22:23:08	2017-01-23 22:26:52
85	RB off	2017-01-23 23:18:22	2017-01-23 23:22:18
86	MB off	2017-01-23 23:23:08	2017-01-23 23:26:52
87	RB off	2017-01-24 00:18:22	2017-01-24 00:22:18
88	MB off	2017-01-24 00:23:08	2017-01-24 00:26:52
89	RB off	2017-01-24 01:18:22	2017-01-24 01:22:18
90	MB off	2017-01-24 01:23:08	2017-01-24 01:26:52
91	RB off	2017-01-24 02:18:22	2017-01-24 02:22:18
92	MB off	2017-01-24 02:23:08	2017-01-24 02:26:52

(Table continued)

TABLE II. *(Continued)*

Nr.	Experiment	Start (UTC)	End (UTC)
93	RB off	2017-01-24 03:18:22	2017-01-24 03:22:18
94	MB off	2017-01-24 03:23:08	2017-01-24 03:26:52
95	RB off	2017-01-24 04:18:22	2017-01-24 04:22:18
96	MB off	2017-01-24 04:23:08	2017-01-24 04:26:52
97	RB off	2017-01-24 05:18:22	2017-01-24 05:22:18
98	MB off	2017-01-24 05:23:08	2017-01-24 05:26:52
99	RB off	2017-01-24 06:18:22	2017-01-24 06:22:18
100	MB off	2017-01-24 06:23:08	2017-01-24 06:26:52
101	RB off	2017-01-24 07:18:22	2017-01-24 07:22:18
102	MB off	2017-01-24 07:23:08	2017-01-24 07:26:52
103	RB off	2017-01-24 09:18:23	2017-01-24 09:22:18
104	MB off	2017-01-24 09:23:08	2017-01-24 09:26:52
105	RB off	2017-01-24 13:18:23	2017-01-24 13:22:18
106	MB off	2017-01-24 13:23:08	2017-01-24 13:26:52
107	RB off	2017-01-24 17:18:23	2017-01-24 17:22:18
108	MB off	2017-01-24 17:23:08	2017-01-24 17:26:52
109	RB off	2017-01-24 21:18:23	2017-01-24 21:22:18
110	MB off	2017-01-24 21:23:08	2017-01-24 21:26:52
111	RB off	2017-01-25 01:18:23	2017-01-25 01:22:18
112	MB off	2017-01-25 01:23:08	2017-01-25 01:26:52
113	RB off	2017-01-25 05:18:23	2017-01-25 05:22:18
114	MB off	2017-01-25 05:23:08	2017-01-25 05:26:52
115	RB off	2017-01-25 08:18:23	2017-01-25 08:22:18
116	MB off	2017-01-25 08:23:08	2017-01-25 08:26:52
117	RB off	2017-01-25 13:48:48	2017-01-25 13:52:43
118	MB off	2017-01-25 13:53:33	2017-01-25 13:57:17
119	RB off	2017-01-25 14:18:23	2017-01-25 14:22:18
120	MB off	2017-01-25 14:23:08	2017-01-25 14:26:52
121	RB off	2017-01-25 20:18:23	2017-01-25 20:22:18
122	MB off	2017-01-25 20:23:08	2017-01-25 20:26:52
123	RB off	2017-01-26 02:18:23	2017-01-26 02:22:18
124	MB off	2017-01-26 02:23:08	2017-01-26 02:26:52
125	RB off	2017-01-26 08:18:23	2017-01-26 08:22:18
126	MB off	2017-01-26 08:23:08	2017-01-26 08:26:52
127	RB off	2017-01-26 14:18:23	2017-01-26 14:22:18
128	MB off	2017-01-26 14:23:08	2017-01-26 14:26:52
129	RB off	2017-01-26 20:18:23	2017-01-26 20:22:18
130	MB off	2017-01-26 20:23:08	2017-01-26 20:26:52
131	RB off	2017-01-27 02:18:23	2017-01-27 02:22:18
132	MB off	2017-01-27 02:23:08	2017-01-27 02:26:52
133	RB off	2017-01-28 12:03:26	2017-01-28 12:07:20
134	MB off	2017-01-28 12:07:55	2017-01-28 12:11:50
135	RB off	2017-02-11 12:03:26	2017-02-11 12:07:45
136	MB off	2017-02-11 12:08:18	2017-02-11 12:12:15
137	RB off	2017-02-12 19:07:45	2017-02-12 19:11:43
138	MB off	2017-02-12 19:12:15	2017-02-12 19:16:14
139	RB off	2017-03-04 12:03:26	2017-03-04 12:07:45
140	MB off	2017-03-04 12:08:18	2017-03-04 12:12:15
141	RB off	2017-03-05 12:03:26	2017-03-05 12:07:45
142	MB off	2017-03-05 12:08:18	2017-03-05 12:12:15
143	RB off	2017-03-18 12:03:26	2017-03-18 12:07:45
144	MB off	2017-03-18 12:08:18	2017-03-18 12:12:15
145	RB off	2017-03-19 12:03:26	2017-03-19 12:07:45
146	MB off	2017-03-19 12:08:18	2017-03-19 12:12:15
147	RB off	2017-04-12 07:05:46	2017-04-12 07:09:40
148	MB off	2017-04-12 07:10:18	2017-04-12 07:14:05
149	RB off	2017-04-29 19:33:22	2017-04-29 19:37:18
150	MB off	2017-04-29 19:37:52	2017-04-29 19:41:40
151	RB off	2017-04-29 23:33:22	2017-04-29 23:37:18
152	MB off	2017-04-29 23:37:52	2017-04-29 23:41:40
153	RB off	2017-04-30 03:33:22	2017-04-30 03:37:18
154	MB off	2017-04-30 03:37:52	2017-04-30 03:41:40
155	RB off	2017-04-30 07:33:22	2017-04-30 07:37:18
156	MB off	2017-04-30 07:37:52	2017-04-30 07:41:40
157	RB off	2017-04-30 11:33:22	2017-04-30 11:37:18
158	MB off	2017-04-30 11:37:52	2017-04-30 11:41:40
159	RB off	2017-04-30 15:33:22	2017-04-30 15:37:18
160	MB off	2017-04-30 15:37:52	2017-04-30 15:41:40
161	RB off	2017-04-30 19:33:22	2017-04-30 19:37:18
162	MB off	2017-04-30 19:37:52	2017-04-30 19:41:40
163	RB off	2017-04-30 23:33:22	2017-04-30 23:37:18
164	MB off	2017-04-30 23:37:52	2017-04-30 23:41:40
165	RB off	2017-05-01 03:33:22	2017-05-01 03:37:18
166	MB off	2017-05-01 03:37:52	2017-05-01 03:41:40
167	RB off	2017-05-01 07:33:22	2017-05-01 07:37:18
168	MB off	2017-05-01 07:37:52	2017-05-01 07:41:40
169	RB off	2017-05-01 19:33:22	2017-05-01 19:37:18
170	MB off	2017-05-01 19:37:52	2017-05-01 19:41:40
171	RB off	2017-05-03 18:33:48	2017-05-03 18:37:38
172	MB off	2017-05-03 18:38:18	2017-05-03 18:42:00
173	RB off	2017-05-18 08:45:48	2017-05-18 08:49:45
174	MB off	2017-05-18 08:50:18	2017-05-18 08:54:15
175	RB off	2017-05-18 13:34:48	2017-05-18 13:38:40
176	MB off	2017-05-18 13:39:15	2017-05-18 13:43:12
177	RB off	2017-05-23 16:03:22	2017-05-23 16:07:15
178	MB off	2017-05-23 16:07:52	2017-05-23 16:11:45
179	RB off	2017-05-24 05:03:22	2017-05-24 05:07:15
180	MB off	2017-05-24 05:07:52	2017-05-24 05:11:45
181	RB off	2017-05-24 18:03:22	2017-05-24 18:07:15
182	MB off	2017-05-24 18:07:52	2017-05-24 18:11:45
183	RB off	2017-05-25 07:03:22	2017-05-25 07:07:15
184	MB off	2017-05-25 07:07:52	2017-05-25 07:11:45
185	RB off	2017-05-27 11:33:22	2017-05-27 11:37:15
186	MB off	2017-05-27 11:37:52	2017-05-27 11:41:45

(Table continued)

TABLE III. Selected and filtered "noise runs" for the long-term noise behavior analysis of the OMS, see Sec. III F.

Nr.	Start (UTC)	End (UTC)
1	2016-03-01 08:05:00	2016-03-02 23:59:59
2	2016-03-03 15:00:00	2016-03-04 20:59:58
3	2016-03-06 18:15:00	2016-03-08 08:00:00
4	2016-03-13 16:30:00	2016-03-15 06:59:59
5	2016-03-16 20:00:00	2016-03-18 23:59:59
6	2016-03-21 02:00:00	2016-03-26 07:59:59
7	2016-03-27 14:00:00	2016-03-28 07:59:58
8	2016-03-29 08:00:00	2016-03-30 07:59:59
9	2016-03-31 08:00:00	2016-04-02 01:59:59
10	2016-04-04 00:00:00	2016-04-14 07:59:59
11	2016-04-26 08:04:00	2016-04-28 07:59:59
12	2016-05-01 08:05:00	2016-05-02 23:54:58
13	2016-05-03 08:00:00	2016-05-05 15:29:59
14	2016-05-13 00:50:00	2016-05-13 07:29:59
15	2016-05-13 08:30:00	2016-05-14 07:59:58
16	2016-05-16 00:00:00	2016-05-19 04:59:59
17	2016-05-19 11:30:00	2016-05-21 10:59:58
18	2016-05-21 15:30:00	2016-05-23 13:59:59
19	2016-05-23 17:03:00	2016-05-25 16:43:59
20	2016-06-06 11:05:00	2016-06-09 07:59:58
21	2016-06-15 13:35:00	2016-06-18 07:58:59
22	2016-06-19 13:00:00	2016-06-24 07:59:59
23	2016-09-19 05:00:55	2016-09-21 12:59:33
24	2016-09-21 13:45:00	2016-09-22 05:55:58
25	2016-09-28 13:35:00	2016-10-01 07:55:58
26	2016-11-09 00:45:19	2016-11-12 07:58:20
27	2016-11-16 11:05:00	2016-11-26 07:59:59
28	2016-12-26 08:00:00	2017-01-13 19:57:59
29	2017-05-28 23:43:55	2017-06-05 14:59:00
30	2017-06-08 12:00:45	2017-06-17 02:55:58

APPENDIX C: ACRONYMS

In this appendix, we provide a list of acronyms used in the main text.

ADC	Analog to digital convertor
AOM	Acousto-optic modulator
ASD	Amplitude spectral density
BH92	Blackmann-Harris-92
CQP	Calibrated quadrant photodiode
DFACS	Drag-free and attitude control system
DMU	Data management unit
DOF	Degree-of-freedom
DPS	Differential power sensing
DRS	Disturbance reduction system
DWS	Differential wave front sensing
EM	Engineering model
ESA	European space agency
FIOS	Fibre injector optical subassembly
FM	Flight model
FPGA	Field programmable gate array
GRS	Gravitational reference sensor
IABG	Industrieanlagen-Betriebsgesellschaft mbH
ITO	indium tin oxide
LISA	Laser interferometer space antenna
LPF	LISA Pathfinder
LPSD	Logarithmic frequency axis power spectral density
MAD	Median absolute deviation
OB	Optical bench
OBF	Optical bench frame
OMS	Optical metrology system
OPD	Optical path length difference
OSTT	On-station thermal tests
OW	Optical window
PD	Photodiode
PLL	Phase locked loop
PM	Phasemeter
PSD	Power spectral density
PZT	Piezo-electric transducer
QPD	Quadrant photodiode
RF	Radio frequency
RIN	Relative intensity noise
SBDFT	Single-bin discrete Fourier transform
SC	Spacecraft
SEP	Solar energetic particles
SNR	Signal-to-noise ratio
SVN	Small vector noise
TM	Test mass
TTL	Tilt-to-length

[1] M. Armano *et al.*, Sensor Noise in LISA Pathfinder: In-Flight Performance of the Optical Test Mass Readout, Phys. Rev. Lett. **126**, 131103 (2021).

[2] F. Antonucci *et al.*, From laboratory experiments to LISA Pathfinder: achieving LISA geodesic motion, Classical Quantum Gravity **28**, 094002 (2011).

[3] F. Antonucci *et al.*, LISA Pathfinder: Mission and status, Classical Quantum Gravity **28**, 094001 (2011).

[4] F. Antonucci *et al.*, The LISA Pathfinder mission, Classical Quantum Gravity **29**, 124014 (2012).

[5] S. Anza *et al.*, The LTP experiment on the LISA Pathfinder mission, Classical Quantum Gravity **22**, S125 (2005).

[6] M. Armano *et al.*, The LISA Pathfinder mission, J. Phys. Conf. Ser. **610**, 012005 (2015).

[7] M. Armano *et al.*, LISA Pathfinder: The experiment and the route to LISA, Classical Quantum Gravity **26**, 094001 (2009).

[8] D. Bortoluzzi *et al.*, Testing LISA drag-free control with the LISA technology package flight experiment, Classical Quantum Gravity **20**, S89 (2003).

[9] P. McNamara *et al.*, The LISA Pathfinder Mission, in *Proceedings of the 9th Lisa Symposium* (Astronomical Society of the Pacific (ASP), California, 2013), Vol. 467, pp. 5–16, https://aspbooks.org/publications/467/005.pdf.

[10] S. Vitale *et al.*, LISA and its in-flight test precursor SMART-2, Nucl. Phys. B, Proc. Suppl. **110**, 209 (2002).

[11] D. Robertson, C. Killow, H. Ward, J. Hough, G. Heinzel, A. Garcia, V. Wand, U. Johann, and C. Braxmaier, LTP interferometer—noise sources and performance, Classical Quantum Gravity **22**, S155 (2005).

[12] M. Armano *et al.*, Sub-Femto-g Free Fall for Space-Based Gravitational Wave Observatories: LISA Pathfinder Results, Phys. Rev. Lett. **116**, 231101 (2016).

[13] M. Armano *et al.*, Beyond the Required LISA Free-Fall Performance: New LISA Pathfinder Results down to $20\,\mu$Hz, Phys. Rev. Lett. **120**, 061101 (2018).

[14] M. Armano *et al.*, Calibrating the system dynamics of LISA Pathfinder, Phys. Rev. D **97**, 122002 (2018).

[15] M. Armano *et al.*, LISA Pathfinder micronewton cold gas thrusters: In-flight characterization, Phys. Rev. D **99**, 122003 (2019).

[16] F. Gibert *et al.*, Thermo-elastic induced phase noise in the LISA Pathfinder spacecraft, Classical Quantum Gravity **32**, 045014 (2015).

[17] M. Armano *et al.*, LISA Pathfinder platform stability and drag-free performance, Phys. Rev. D **99**, 082001 (2019).

[18] J. I. Thorpe *et al.*, Micrometeoroid events in LISA Pathfinder, Astrophys. J. **883**, 53 (2019).

[19] P. Amaro-Seoane *et al.*, Laser interferometer space antenna, arXiv:1702.00786.

[20] A. Schleicher, T. Ziegler, R. Schubert, N. Brandt, P. Bergner, U. Johann, W. Fichter, and J. Grzymisch, In-orbit performance of the LISA Pathfinder drag-free and attitude control system, CEAS Space J. **10**, 471 (2018).

[21] F. Antonucci *et al.*, The LISA Pathfinder mission, Classical Quantum Gravity **29**, 124014 (2012).

[22] H. Audley *et al.*, The LISA Pathfinder interferometry—hardware and system testing, Classical Quantum Gravity **28**, 094003 (2011).

[23] G. Heinzel, C. Braxmaier, R. Schilling, A. Rudiger, D. Robertson, M. T. Plate, V. Wand, K. Arai, U. Johann, and K. Danzmann, Interferometry for the LISA technology package (LTP) aboard SMART-2, Classical Quantum Gravity **20**, S153 (2003).

[24] G. Heinzel *et al.*, The LTP interferometer and phasemeter, Classical Quantum Gravity **21**, S581 (2004).

[25] C. Braxmaier *et al.*, LISA Pathfinder optical interferometry, in Gravitational wave and particle astrophysics detectors, in *Proceedings of the Society of Photo-Optical Instrumentation Engineers (SPIE)*, edited by J. Hough and G. H. Sanders (SPIE, USA, 2004), Vol. 5500, pp. 164–173, 10.1117/12.555266.

[26] D. Robertson, 3OB "As Built" OptoCAD model, Institute for Gravitational Research, University of Glasgow Technical Report No. S2-UGL-TN-3045, 2013.

[27] E. Morrison, B. J. Meers, D. I. Robertson, and H. Ward, Experimental demonstration of an automatic alignment system for optical interferometers, Appl. Opt. **33**, 5037 (1994).

[28] E. Morrison, B. J. Meers, D. I. Robertson, and H. Ward, Automatic alignment of optical interferometers, Appl. Opt. **33**, 5041 (1994).

[29] M. Dehne, M. Troebs, G. Heinzel, and K. Danzmann, Verification of polarising optics for the LISA optical bench, Opt. Express **20**, 27273 (2012).

[30] P. Canizares *et al.*, The LISA Pathfinder DMU and radiation monitor, Classical Quantum Gravity **28**, 094004 (2011).

[31] K. F. Middleton *et al.*, Prototype optical bench instrument in the interferometer for the LISA-Pathfinder space mission, Opt. Eng. **45**, 125601 (2006).

[32] G. Heinzel *et al.*, Successful testing of the LISA Technology Package (LTP) interferometer engineering model, Classical Quantum Gravity **22**, S149 (2005).

[33] A. Monsky, Understanding interferometric drag-free sensors in space using intelligent data analysis tools, Ph.D. thesis, Leibniz University, Hannover, 2010, 10.15488/7478.

[34] L. Wissel, A. Wittchen, T. S. Schwarze, M. Hewitson, G. Heinzel, and H. Halloin, Relative-Intensity-Noise Coupling in Heterodyne Interferometers, Phys. Rev. Applied **17**, 024025 (2022).

[35] A. F. G. Marin, V. Wand, F. Steier, F. G. Cervantes, J. Bogenstahl, O. Jennrich, G. Heinzel, and K. Danzmann, On-orbit alignment and diagnostics for the LISA technology package, Classical Quantum Gravity **23**, S133 (2006).

[36] F. G. Cervantes, F. Steier, G. Wanner, G. Heinzel, and K. Danzmann, Subtraction of test mass angular noise in the LISA technology package interferometer, Appl. Phys. B **90**, 395 (2008).

[37] G. Wanner and N. Karnesis, Preliminary results on the suppression of sensing cross-talk in LISA Pathfinder, J. Phys. Conf. Ser. **840**, 012043 (2017).

[38] A. F. Garcin Marin *et al.*, Interferometric characterization of the optical window for LISA Pathfinder and LISA, AIP Conf. Proc. **873**, 344 (2006)..

[39] M. Nofrarias, A. F. G. Marin, A. Lobo, G. Heinzel, J. Ramos-Castro, J. Sanjuan, and K. Danzmann, Thermal diagnostic of the optical window on board LISA Pathfinder, Classical Quantum Gravity **24**, 5103 (2007).

[40] D. I. Robertson *et al.*, Construction and testing of the optical bench for LISA Pathfinder, Classical Quantum Gravity **30**, 085006 (2013).
[41] C. J. Killow, J. Bogenstahl, F. Guzmán Cervantes, M. Perreur-Lloyd, D. I. Robertson, F. Steier, and H. Ward, Construction of the LTP Optical Bench Interferometer, AIP Conf. Proc. **873**, 297 (2006).
[42] C. J. Killow, E. D. Fitzsimons, J. Hough, M. Perreur-Lloyd, D. I. Robertson, S. Rowan, and H. Ward, Construction of rugged, ultrastable optical assemblies with optical component alignment at the few microradian level, Appl. Opt. **52**, 177 (2013).
[43] E. Fitzsimons, Optical characterisation of 3OB (S2–UGL–TN–3039), University of Glasgow Technical Report, 2013.
[44] H. Ward, Optical bench interferometer detailed design, Institute for Gravitational Research, University of Glasgow Technical Report No. S2-UGL-DDD-3003, 2007.
[45] C. J. Killow, E. D. Fitzsimons, M. Perreur-Lloyd, D. I. Robertson, H. Ward, and J. Bogenstahl, Optical fiber couplers for precision spaceborne metrology, Appl. Opt. **55**, 2724 (2016).
[46] H. Ward, OBI—Revised fibre injector design, Institute for Gravitational Research, University of Glasgow Technical Report No. S2-UGL-DDD-3004, 2008.
[47] D. Robertson, OBI FMECA, Institute for Gravitational Research, University of Glasgow Technical Report No. S2-UGL-DDD-3001, 2007.
[48] A. M. Cruise, D. Hoyland, and S. M. Aston, Implementation of the phasemeter for LISA LTP, Classical Quantum Gravity **22**, S165 (2005).
[49] L. Gesa, V. Martin, A. Conchillo, A. Lobo, and I. Lloro, The LISA PathFinder DMU software, a global overview, in *Proceedings of the 9th Lisa Symposium* (Astronomical Society of the Pacific (ASP), California, 2013), Vol. 467, pp. 277–278, https://aspbooks.org/publications/467/277.pdf.
[50] A. Lobo *et al.*, Data and diagnostics in LISA PathFinder, AIP Conf. Proc. **841**, 489 (2006).
[51] G. Hechenblaikner and others, Digital laser frequency control and phase-stabilization loops in a high precision space-borne metrology system, IEEE J. Quantum Electron. **47**, 651 (2011).
[52] F. G. Cervantes *et al.*, LISA technology package flight hardware test campaign, in *Proceedings of the 9th Lisa Symposium* (Astronomical Society of the Pacific (ASP), California, 2013), Vol. 467, pp. 141–150, https://www.aspbooks.org/publications/467/141.pdf.
[53] M. Hewitson *et al.*, Data analysis for the LISA technology package, Classical Quantum Gravity **26**, 094003 (2009).
[54] M. Tröbs and G. Heinzel, Improved spectrum estimation from digitized time series on a logarithmic frequency axis, Measurement **39**, 120 (2006).
[55] G. Heinzel, A. Rüdiger, and R. Schilling, Spectrum and spectral density estimation by the Discrete Fourier Transform (DFT), including a comprehensive list of window functions and some new flat-top windows (2002), https://pure.mpg.de/rest/items/item_152164_2/component/file_152163/content.
[56] G. Anderson *et al.*, Experimental results from the ST7 mission on LISA Pathfinder, Phys. Rev. D **98**, 102005 (2018).
[57] M. Armano *et al.*, Capacitive sensing of test mass motion with nanometer precision over millimeter-wide sensing gaps for space-borne gravitational reference sensors, Phys. Rev. D **96**, 062004 (2017).
[58] M. Kersten, Test report on OMS performance parameter characterization during OSTT, Astrium Technical Report No. S2-ASD-TR-3155, 2012.
[59] S. Paczkowski, Laser frequency stabilisation and interferometer path length differences during the LISA Pathfinder satellite mission, Ph.D. thesis, Leibniz Universität Hannover, 2021, 10.15488/11130.
[60] A. Wittchen, Relative intensity noise in the LISA Pathfinder interferometer—experiments on ground and in space, Ph.D. thesis, Hannover, 2021, 10.15488/11700.
[61] H. Audley, Preparing for LISA Pathfinder operations: Characterisation of the optical metrology system, Ph.D. thesis, Leibniz Universität Hannover, 2014, 10.15488/8220.
[62] A. Cavalleri, G. Ciani, R. Dolesi, A. Heptonstall, M. Hueller, D. Nicolodi, S. Rowan, D. Tombolato, S. Vitale, P. J. Wass, and W. J. Weber, Increased Brownian Force Noise from Molecular Impacts in a Constrained Volume, Phys. Rev. Lett. **103**, 140601 (2009).
[63] M.-S. Hartig, S. Schuster, and G. Wanner, Geometric tilt-to-length coupling in precision interferometry: Mechanisms and analytical descriptions, J. Optics **24**, 065601 (2022).
[64] H. Audley *et al.*, LISA Pathfinder mission extension report for the German contribution, Max Planck Institute for Gravitational Physics (Albert Einstein Institute) Technical Report No. 50OQ1601, 2020, 10.2314/KXP:1692401564.
[65] G. Heinzel *et al.*, LPF final report for the German contribution to the nominal mission, Max Planck Institute for Gravitational Physics (Albert Einstein Institute) Technical Reports No. 50OQ0501 and No. LPF-RP-2017-01-01, 2018, 10.2314/GBV:1030758840.
[66] M. Armano *et al.*, Temperature stability in the sub-milli-Hertz band with LISA Pathfinder, Mon. Not. R. Astron. Soc. **486**, 3368 (2019).
[67] M.-S. Hartig, N. Karnesis, L. Tevlin, and G. Wanner, Tilt-to-length coupling in LISA Pathfinder: A data analysis (to be published).
[68] M.-S. Hartig and G. Wanner, Tilt-to-length coupling in LISA Pathfinder: Analytical modelling (to be published).
[69] LISA Pathfinder Collaboration, Transient acceleration events in LISA Pathfinder: Properties and possible physical origin, arXiv:2205.11938.
[70] Q. Baghi, N. Korsakova, J. Slutsky, E. Castelli, N. Karnesis, and J.-B. Bayle, Detection and characterization of instrumental transients in LISA Pathfinder and their projection to LISA, Phys. Rev. D **105**, 042002 (2022).
[71] S. Vitale *et al.*, Data series subtraction with unknown and unmodeled background noise, Phys. Rev. D **90**, 042003 (2014).
[72] B. Kaune, In-orbit stability analysis of the LISA pathfinder optical metrology: Photoreceivers and polarisation, Ph.D. thesis, Leibniz Universität Hannover, 2021, 10.15488/10887.

[73] C. Grimani, D. Telloni, S. Benella, A. Cesarini, M. Fabi, and M. Villani, Study of galactic cosmic-ray flux modulation by interplanetary plasma structures for the evaluation of space instrument performance and space weather science investigations, Atmosphere-Ocean **10**, 749 (2019).

[74] C. Grimani, A. Cesarini, M. Fabi, F. Sabbatini, D. Telloni, and M. Villani, Recurrent galactic cosmic-ray flux modulation in l1 and geomagnetic activity during the declining phase of the solar cycle 24, Astrophys. J. **904**, 64 (2020).